

TRAJECTORY OPTIMIZATION STRATEGIES FOR SUPERCAVITATING VEHICLES

A Thesis
Presented to
The Academic Faculty

by

Rahul Kamada

In Partial Fulfillment
of the Requirements for the Degree
Master of Science

School of Aerospace Engineering
Georgia Institute of Technology
November 2005

TRAJECTORY OPTIMIZATION STRATEGIES FOR SUPERCAVITATING VEHICLES

Approved by:

Professor M. Ruzzene, Adviser

Professor Carlo L. Bottasso

Professor John R. Olds

Date Approved: November 15, 2004

ACKNOWLEDGEMENTS

I extend my sincere gratitude and appreciation to the people who made this masters thesis possible. Special thanks are due to my advisor Professor Massimo Ruzzene for his patience and guidance throughout this work. I would also like to thank Professor Carlo Bottasso for his advice and suggestions in many parts of this study. I also appreciate Professor John R. Olds for his suggestions for further work and for participating in my thesis evaluation committee.

I would also like to acknowledge the financial support from the Office of Naval Research.

TABLE OF CONTENTS

ACKNOWLEDGEMENTS	iii
LIST OF TABLES	vi
LIST OF FIGURES	vii
SUMMARY	ix
I INTRODUCTION	1
1.1 Overview	1
1.2 Introduction to cavitation and supercavitation	3
1.3 Related research	5
1.4 Motivations and Objectives	6
1.5 Trajectory optimization	8
1.6 Organization of the thesis	9
II MODEL OF SUPERCAVITATING VEHICLE DYNAMICS	11
2.1 Introduction	11
2.2 Vehicle configuration	12
2.3 Equations of motion	14
2.4 Forces	16
2.4.1 Cavity shape and dimensions	17
2.4.2 Nose-water interactions	18
2.4.3 Fin Forces	19
2.4.4 Penetration distance	23
2.4.5 Tail-cavity Interaction forces - Simplified Approach	23
2.4.6 Tail-cavity Interaction forces - Kulkarni and Pratap	24
2.4.7 Tail-cavity Interaction forces - Hassan Theory	27
III TRAJECTORY OPTIMIZATION	32
3.1 Overview	32
3.2 Optimization Techniques	32
3.2.1 Direct and Indirect Methods: Single DOF Problem	34
3.3 The Optimal Control Problem For the Supercavitating Torpedo	38

3.4	Numerical Solution	39
3.5	Methods Employed to Improve Convergence	41
3.5.1	Bootstrap technique	41
3.5.2	Scaling the variables	44
3.5.3	Method of “continuation”	45
3.6	TOMLAB and SNOPT	46
IV	NUMERICAL SIMULATION AND RESULTS	49
4.1	Overview	49
4.2	Control Effort	50
4.2.1	Dive maneuvers	50
4.2.2	Turn maneuvers	54
4.3	Control Velocity	56
4.3.1	Dive maneuvers	56
4.4	Comparison of Control Velocity and Control Effort Cases	60
4.5	Stationary Obstacle Circumvention	61
4.5.1	Modelling the Obstacle	61
4.5.2	Formulation of Obstacle as a Constraint	61
4.5.3	Vertical Infinite Elliptical Cylinder Obstacle Avoidance	65
4.5.4	Horizontal Infinite Elliptical Cylinder Obstacle Avoidance	69
4.6	Effect of Cavitation Number on Maneuvers	72
V	CONCLUDING REMARKS	76
5.1	Conclusions	76
5.2	Further Work	77
5.2.1	Complex maneuvers	77
5.2.2	Real-time controller	77
5.2.3	Investigating flight envelopes	77
5.2.4	Flexible-body flight simulations	78
	REFERENCES	79

LIST OF TABLES

1	Dimensions of torpedo.	14
---	--------------------------------	----

LIST OF FIGURES

1	Illustration of the Russian Shkval torpedo.	2
2	Three prominent phases of vehicle motion.	5
3	Configuration of the supercavitating vehicle.	11
4	Configuration of supercavitating vehicle with applied forces.	12
5	View of cruciform arrangement of fins (view from behind the vehicle)	13
6	Body-fixed and inertial frames.	15
7	Cavity dimensions calculated using Reichardt formulation.	18
8	Cavitator reference frame.	20
9	Fin reference frame and angle of attack.	21
10	Fin force coefficients versus angle of attack, for varying penetration depth. .	22
11	Calculation of fin penetration depth.	24
12	Impact force and moment calculation.	25
13	Partly immersed tail section.	27
14	Immersion of the cylindrical profile in water.	28
15	Planing of the cylinder on the cavity surface.	29
16	Nodes and intervals	35
17	Optimized displacement and analytical solution	36
18	Magnitude of error vs. number of nodes used	37
19	Schematic diagram explaining bootstrap procedure.	42
20	Bootstrap procedure projecting data onto finer grid.	43
21	Convergence of solution as a result of bootstrap technique.	43
22	Application of continuation technique to arrive at dive of 60 m using a better starting guess (i.e. solution to 50 m dive problem).	46
23	Sparsity pattern of the Jacobian matrix for our problem.	48
24	Family of dives with increasing final depth.	51
25	Control time history for 10 m (dashed line) and 60 m dives (solid line). . .	52
26	Inertial orientations for 10 m (dashed line) and 60 m dives (solid line). . . .	53
27	Vehicle trajectories for a family of turns	54
28	Control time history for 60° (dashed line) and 180° turns (solid line)	55

29	Inertial orientations for 60° (solid line) and 180° turns (dashed line)	55
30	Vehicle trajectories for a family of dives with control velocity as the objective function	57
31	Control time history for 10 m (dashed line) and 60 m dives (solid line) for control velocity minimization case.	58
32	Inertial orientations for 10 m (dashed line) and 60 m dives (solid line) for control velocity minimization case	59
33	Control time history for 60 m dives with control velocity minimization (dashed line) and control effort minimization (solid line)	60
34	Enveloping the arbitrary cross-section in an ellipse	62
35	Using a step-function to assign trajectory constraint violation	63
36	Using the Gaussian function to assign trajectory constraint violation	64
37	Gaussian function at each node of the grid	65
38	Gaussian function for an infinite elliptical cylinder obstacle in the $\mathbf{u}_P(3) = 0$ plane	66
39	Feasible vehicle trajectory avoiding vertical cylindrical obstacle	66
40	Inertial orientations for vertical cylinder avoidance case	67
41	Control time history for vertical cylinder avoidance case.	68
42	Gaussian function for an infinite elliptical cylinder obstacle in the $\mathbf{u}_P(2) = 0$ plane	69
43	Feasible vehicle trajectory avoiding horizontal cylindrical obstacle	70
44	Inertial orientations for horizontal cylinder avoidance case	70
45	Control time history for horizontal cylinder avoidance case.	71
46	Variation of σ with increasing depth and increasing velocity	73
47	Variation of d_{max} and l_c with increasing σ	73
48	Variation of σ with increasing depth underwater (3-D plot)	74
49	Variation of σ with increasing depth underwater (2-D plot)	74
50	A 15 degree turn maneuver at varying depths.	75

SUMMARY

Supercavitating vehicles are characterized by substantially reduced hydrodynamic drag with respect to fully wetted underwater vehicles. Drag is localized at the nose of the vehicle, where a cavitator generates a cavity that completely envelops the body. This causes the center of pressure to be always ahead of the center of mass, thus violating a fundamental principle of hydrodynamic stability. This unique loading configuration, the complex and non-linear nature of the interaction forces between vehicle and cavity, and the unsteady behavior of the cavity itself make the control and maneuvering of supercavitating vehicles particularly challenging. This study represents an effort towards the evaluation of optimal trajectories for this class of underwater vehicles, which often need to operate in unsteady regimes and near the boundaries of the flight envelope.

Flight trajectories and maneuvering strategies for supercavitating vehicles are here obtained through the solution of an optimal control problem. Given a cost function and general constraints and bounds on states and controls, the solution of the optimal control problem yields the control time histories that maneuver the vehicle according to a desired strategy, together with the associated flight path. The optimal control problem is solved using the direct transcription method, which does not require the derivation of the equations of optimal control and leads to the solution of a discrete parameter optimization problem. Examples of maneuvers and resulting trajectories are given to demonstrate the effectiveness of the proposed methodology and the generality of the formulation.

Chapter I

INTRODUCTION

1.1 Overview

Underwater vehicles such as torpedoes and submarines are limited in maximum speed by the considerable drag produced by the skin friction on the hull. Speeds of 40m/s are considered as a maximum limit in most applications, and most practical systems are limited to less than half this value [22]. The primary reason for these low speeds is the large component of skin friction drag. When a body moves in a fluid, a layer of the fluid clings to the surface of the body and is dragged with it. This interaction causes high drag forces on the body and is commonly termed skin friction drag. The net drag force in water is dominated by the skin friction drag component as compared to other sources such as pressure drag. In fact, water produces up to 1000 times more drag resistance than air does. While low speed is advantageous for acoustics and hydrodynamic efficiency, in certain applications higher speeds are desirable for underwater vehicles and projectiles. Significantly higher speeds cannot be obtained by just streamlining the body or improving the propulsion system. These solutions provide some improvements in speed but no considerable reduction in skin friction drag.

A phenomenal improvement in speed and reduction in skin friction drag is possible through supercavitation. When a body moves through water at sufficient speed, the fluid pressure drops locally below the level that sustains the liquid phase, and a low-density gaseous cavity forms. In other words, if there is not enough pressure to hold them together, the liquid molecules of water dissociate into a gas. Flows exhibiting cavities that entirely envelop the moving body are called "supercavitating." In supercavitating flows, the liquid phase does not contact the moving body over most of its length, thus making the skin friction drag almost negligible. Several new and projected supercavitating underwater vehicles exploit supercavitation as a means to achieve extremely high submerged speeds and low

drag. The size of existing or notional supercavitating high-speed bodies ranges from that of projectiles to heavyweight full-scale torpedoes. An example of a primitive version of this technology is the Shkval torpedo developed in the 1970s, shown in figure 2.

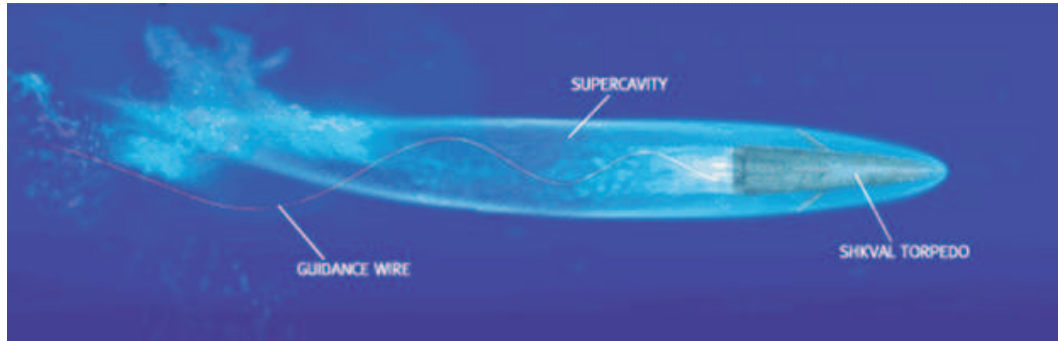


Figure 1: Illustration of the Russian Shkval torpedo.

The RAMICS (Rapid Airborne Mine Clearance System) project aims to neutralize near surface mines. The RAMICS supercavitating projectile is small, bullet-like, flat-nosed and spin stabilized in air. The projectile is designed to enter the water at oblique angles to the surface and to travel in both air and water. Upon water entry the shape and speed of the projectile produce a cavitation envelope in which the projectile rides at low drag. These projectiles can travel far greater distances underwater than conventional bullets and can effectively neutralize shallow bottom mines.

The AHSUM (Adaptable High-Speed Undersea Munitions) technology is an entirely subsurface gun system taking the form of supercavitating "kinetic-kill" bullets that are fired from guns in streamlined turrets fitted to the submerged hulls of submarines, surface ships or towed mine-countermeasure sleds. The sonar-directed AHSUM system aims to protect vessels from incoming undersea cruise missiles.

Both the RAMICS and the AHSUM are uncontrolled small range supercavitating projectiles. The next higher level of supercavitating projectiles is larger torpedoes with higher speeds and longer ranges. The Russian Shkval is the foremost example of a first-generation design of a supercavitating torpedo. It is considered to be somewhat crude and unrefined because it is unguided, it can only travel along a straight trajectory and it has a range of about 5 miles. There are no control surfaces on the torpedo and only warhead detonation

and some other minor weapon operations can be controlled.

More advanced supercavitating vehicles would be larger with higher speeds and greater maneuverability. These vehicles require the design of a special launch station. Detailed studies of hydrodynamics, acoustics, guidance and control and propulsion are involved in the development of these systems. This is the kind of vehicle that is studied in this work.

1.2 Introduction to cavitation and supercavitation

Water is a nearly incompressible medium whose properties change marginally even for great changes in pressure. However when its pressure drops below the saturated vapor pressure (at a given temperature) discontinuities arise in the form of bubbles, foils and cavities. These formations are filled with water vapor. This resembles in appearance, the phenomenon of boiling of water. But the bubbles generated during boiling are stable and they either escape to the surface or release their heat to the surrounding liquid. In the latter case the bubble fills with water as the gas inside the bubble gradually condenses. On the other hand, the bubbles formed during cavitation depend on the low pressure of the surrounding liquid to survive. As the pressure of the surrounding liquid increases there comes a point when the cavity collapses suddenly and catastrophically. This violent implosion of cavities creates shock waves that dig pits in exposed metal, scarring propeller blades and pipes.

Cavitating flows are commonly described by the cavitation number σ . The cavitation number is a measure of the tendency of cavitation to occur in a flow and as such, it is a principal quantity governing cavity dimensions. It is formally defined in section 2. According to the size of σ three cavitation stages are defined:

(1) High cavitation numbers ($1.1 \geq \sigma \geq 1.6$ [26]): Initial cavitation which is always the bubble stage and it is accompanied by the strong characteristic noise of collapsing bubbles and a strong erosive property, with the ability to destroy solid material such as blades of screws, pumps and turbines.

(2) Moderate cavitation numbers ($0.5 \geq \sigma \geq 1.1$): Partial cavitation, during which the arising cavities cover a cavitating body part. The cavity exhibits random pulsations and fluctuations and is unstable.

(3) Low cavitation numbers ($\sigma \leq 0.39$): Fully developed cavitation or supercavitation during which the cavity dimensions exceed those of the body.

In supercavitation, the bubble is longer than the object, so that only its leading edge is in contact with liquid water.

A supercavity can be maintained through:

(1) Vaporous cavitation: The speed of the body is sufficiently high to vaporize the fluid around it.

(2) Artificial cavitation: Gas is constantly supplied to the cavity at nearly ambient pressure.

When the body is enveloped by a cavity of water vapor such that only its nose is in contact with liquid water, the skin friction drag is substantially reduced. This reduced skin friction drag means that supercavitating vehicles can attain much higher speeds than conventional vehicles for the same amount of propulsive force.

The three prominent phases of vehicle motion within the cavity envelope are:

(1) 'riding' the cavity with only the vehicle nose being in contact with the cavity boundary

(2) planing along the lower internal cavity surface as a means of vehicle weight balance at low velocities (50m/s to 200m/s) and

(3) impact interaction (tail-slap) with the cavity boundaries due to initial perturbations in the velocity of the vehicle.

As the vehicle slows down, its cavitation number increases and the size of the vapor cavity decreases until it disappears. Unlike a normal cavity, the death of a supercavity surrounding a projectile is not sudden or violent. The cavity simply shrinks around the projectile at an ever-increasing rate until the cavity no longer exists. There is little or no damage to the vehicle from supercavity collapse, a crucial advantage over the craters left by cavitation [26].

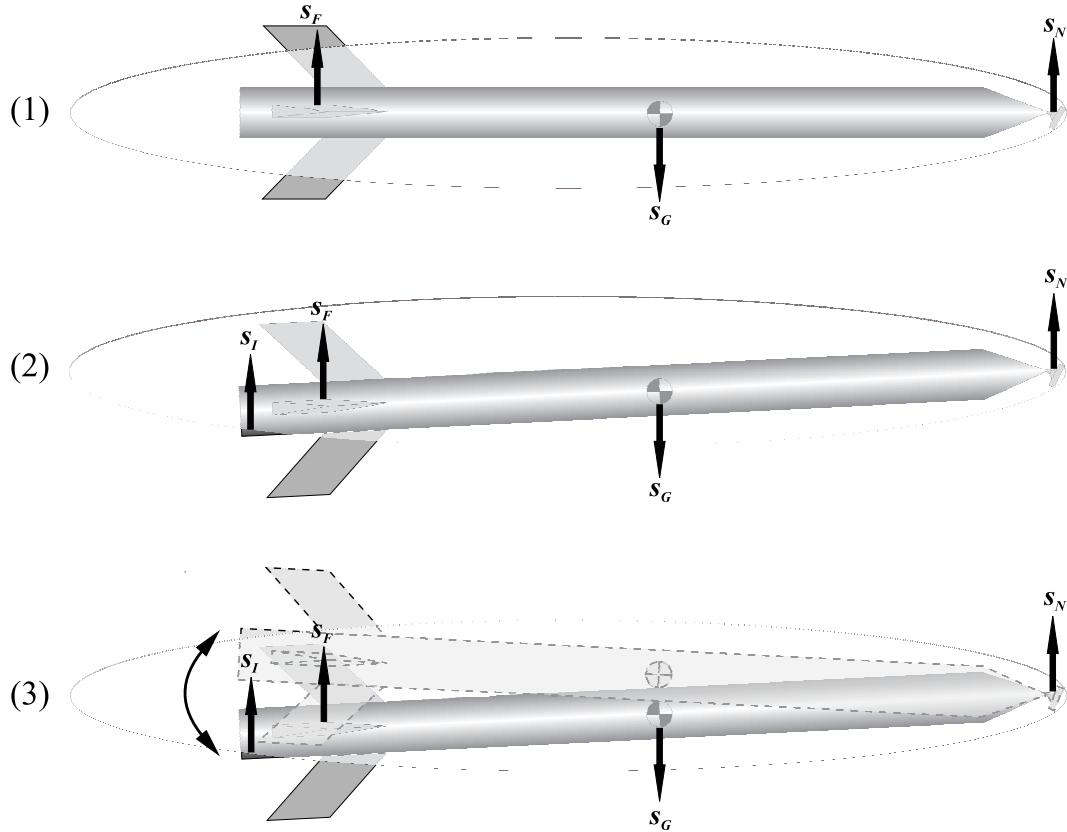


Figure 2: Three prominent phases of vehicle motion.

1.3 Related research

Research in the field of cavitation and supercavitation and studies on the forces acting on cavitating bodies have been carried out as far back as the 1920s. For example Brodetsky [8] studied discontinuous fluid motion past circular and elliptic cylinders. In the 1940s and 1950s focus shifted to solving problems of water entry without ricochets and planing [23]. Other problems of interest involved avoidance of the phenomenon of cavitation in supercavitating ship screws, pumps and hydrofoils (Posdunin [4], Tulin [27]).

The work by May [19] contains an extensive collection of parametric experimental data for different forces on different supercavitating shapes. Graphical data on the coefficients of lift and drag for various cavitating shapes such as disks, cones, ogives and wedges is provided for different cavitation numbers. More recently, the CFD database provided in Fine [7] contains values for coefficients of lift and drag for conical cavitators which are functions of

the half angle of the cone and the angle of attack. This database also has coefficients of lift and drag for wedges as a function of the wetted surface and its geometrical properties. This data is used in the work for the calculation of fin forces for the torpedo.

In the late 1990s studies were performed on the dynamics of supercavitating vehicles. Kulkarni and Pratap [8] and Rand et al. [9] studied the dynamics of uncontrolled supercavitating projectiles. A dynamic model for RAMICS and AHSUM was developed. It was shown that the projectile rotates or precesses inside the cavity. This precession leads to impacts between the tail of the projectile and the cavity wall. The frequency of the impact increases with time and the resulting drag slows the projectile down thus reducing the range and time of flight of the projectile to the order of a few seconds.

Dzielski and Kurdila [16] consider the formulation of a benchmark control problem for a supercavitating torpedo. They also develop a dynamical model for a fin-controlled torpedo which includes a formulation for the cavity. Their observations indicate that the weight of the body causes it to bounce or skip inside the walls of the cavity causing instability. They present a control system design and the corresponding results of closed-loop simulations.

Kirschner et al. [14] present control strategies for the highly coupled nonlinear system comprising a supercavitating vehicle. A banked maneuvering strategy was proposed in consideration of the system of forces acting on the vehicle and to maintain mechanical simplicity of the cavitator. A feed-forward control model was developed and trajectory stability and dynamic behavior was investigated for straight and level flight and for maneuvering. It was shown that the system eigenvalues depend strongly on the type of afterbody support specified for the vehicle (planing or non-planing) but that their 7-state controller could eliminate undesirable behavior in either case.

1.4 Motivations and Objectives

Supercavitating bodies achieve stability through their interaction with the fluid surrounding the cavity. Bodies moving between 50 to 200 m/s typically "plane" along the internal surface of the cavity while periodic impacts ("tail-slaps") with the interior surface occur at higher speeds of about 300 to 400 m/s. Vehicles equipped with control surfaces such as fins and a

tail are stabilized by balancing forces acting on these surfaces. These interactions between the vehicle and the water/cavity are sources of structural strains and vibrations and they also affect the guidance and trajectory of the vehicle.

In order to design a control system for these vehicles, to predict their trajectories and to simulate their motion in forward dynamics these systems must be cast into mathematical models and analyzed. However, for this type of underwater vehicles there are special conditions that make modelling and control a challenge. The main difficulties of using the supercavitating flow scheme for underwater objects are related to the necessity of ensuring the object's motion stability in conditions where there is a loss of Archimedean buoyancy forces. The location of the center of pressure being well forward of the center of gravity poses further problems for stability. Further, while a fully wetted vehicle develops substantial lift in turn due to vortex shedding off the hull, a supercavitating vehicle does not develop significant lift over the gas-enveloped surfaces. In addition the cavity-vehicle interaction is nonlinear and exhibits strong memory effects related to the cavity shape being a function of the history of the vehicle motion. These distinct operating conditions and sources of non-linearities give rise to unique challenges for flight mechanics simulators for this class of vehicles.

In view of the above challenges, this work aims to address the problem of modelling and simulation of such vehicles and also the problem of guidance, control and design. For this class of vehicles achieving aggressive maneuverability and maximizing steady flight performance is one of the primary goals in design. We address the problem of trajectory optimization as a first step towards this goal. We find the flight envelope of the vehicle using the trajectory optimization tools, given the configuration of the vehicle and other operational parameters.

The functionalities provided by the methodology described in the following sections will later on be used for:

(a) investigating the vehicle performance in the maneuvering flight regime. We calculate optimal trajectories for certain maneuvers and study the time history of the controls, the vehicle displacements and orientations.

(b) actual guidance of the vehicle, whereby a real-time controller tracks the optimal trajectory and regulates and stabilizes the vehicle against deviations from this trajectory. Trajectories generated a-priori, for example by interpolation of way-points, are typically not compatible with the vehicle dynamics. For high performance vehicles such as the ones here considered, this can imply that the real-time controller might be unable to effectively realize the desired trajectory, or the flight may result in excessive loads or in high frequency oscillations and repeated impact interactions between the vehicle and the cavity, which are clearly all undesirable effects.

(c) comparing the response of a flexible-body forward dynamics simulation [10] with the results obtained from the rigid-body forward dynamics simulations and the trajectory optimization tools.

1.5 Trajectory optimization

The particular question of interest that is addressed in this work with regards to supercavitating vehicles is how to select a time-dependent control function that minimizes a certain objective function and yet satisfies a number of path and boundary conditions. Given a performance index (objective function) and general constraints and bounds on the states and controls that translate the flight envelope limitations of the vehicle and the necessary safety requirements, what control time-history and flight path will take the vehicle from point A to point B according to the prescribed criteria. Given the complexity of the dynamics of this system, it is important to design optimized maneuvers prior to performing field tests or physical experiments. This would help to predict and avoid unforeseeable violations of flight envelopes and accidentally engaging in unsafe maneuvers.

There are two different categories of methods used in the field of trajectory optimization (Betts [2]):

- (1) Indirect methods, based on the calculus of variations and
- (2) Direct methods, based on transcription methods and Non Linear Problem (NLP) solvers.

While indirect methods give extremely accurate results and additional information about

optimality, they usually involve specialized mathematical analysis for each single problem. Results are usually very specialized on a very specific problem, and changes to this problem often require a lot of effort to be incorporated in existing solutions. Application of the calculus of variation to a trajectory optimization problem usually leads to a so-called multi-point boundary value problem which has to be solved using a multi-dimensional zero-finding algorithm.

In contrast, direct methods are very general in their approach, but usually lead to suboptimal solutions. However, such solutions can be achieved without additional labor in the framework of complicated mathematical analysis of each problem. Direct methods supply a very general approach for a large variety of trajectory optimization problems. The transcription process renders the problem finite-dimensional and then discrete optimization of a discrete non-linear programming problem is conducted.

Optimal control problems are boundary value problems, rather than initial value problems as in the case of the classical forward-in-time integration of the equations of dynamic equilibrium. This means that the solution is potentially expensive to compute. Furthermore, these problems are often highly non-linear and notoriously difficult to solve, so that robust numerical methods become of primary importance. We use direct methods to solve our optimization problem, with the advantage that these methods are highly robust and they guarantee the broad applicability of the simulation tools to the widest possible variety of situations.

1.6 Organization of the thesis

The objective of this work is to provide a designer with optimal controls required to maneuver supercavitating torpedoes. Tools are designed to calculate optimal trajectories for maneuvers between any two points. Simulations and visualization of the motion of the projectile are performed.

Chapter 2 describes the model of the supercavitating vehicle dynamics which has been adopted in this study. The configuration of the torpedo and its interactions with the cavity are described.

In chapter 3 the optimization procedures and methodologies employed are explained. We describe the optimal control problem and strategies used to solve it. Since optimization problems require a good starting guess, the methods used to improve convergence are outlined.

We specify torpedo dimensions and other simulation parameters in chapter 4. We also explain the exploitation of the sparsity pattern of the constraint gradient matrices to improve computation time. Two different objective functions are presented and we justify their physical significance. We then present some results and comparisons of the numerical simulations conducted.

Finally conclusions of this study and avenues for future work are delineated in chapter 5.

Chapter II

MODEL OF SUPERCAVITATING VEHICLE DYNAMICS

2.1 Introduction

Supercavitation is a very useful phenomenon for drag reduction for torpedoes, but it presents significant challenges in modelling and control. Since a significant portion of the vehicle is located in the cavity, the control, guidance and stability of the torpedo must be managed by very small control surface regions in the front and aft of the vehicle. The primary issues associated with the operating conditions of supercavitating vehicles may be summarized as:

- (1) generation and maintenance of cavity,
- (2) balancing the weight of the vehicle,
- (3) control and guidance,
- (4) stability.

A sketch of the supercavitating torpedo is presented in figure 3 . The main parts of the torpedo are the cavitator in the front and the four fins in the aft portion of the torpedo. The cavitator is used to generate and maintain the cavity. The cavitator and the four fins together are also used for control and stability of the vehicle.

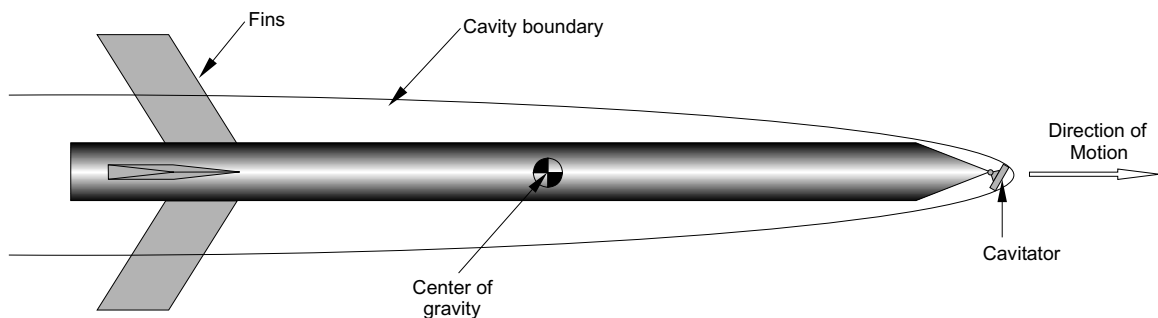


Figure 3: Configuration of the supercavitating vehicle.

2.2 Vehicle configuration

The candidate vehicle configuration considered for this study consists of two important control surfaces, the cavitator and the fins. A schematic of the vehicle configuration and of the applied forces is shown in figure 4. The body is acted upon by a system of forces corresponding to the interaction of the vehicle control surfaces with the cavity boundaries.

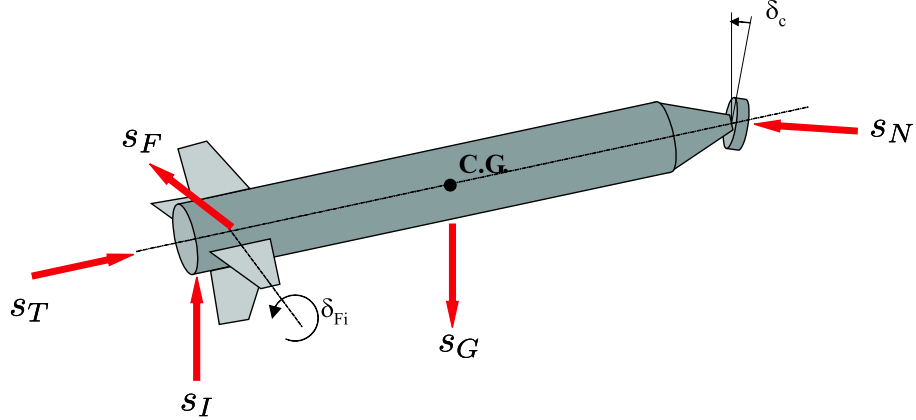


Figure 4: Configuration of supercavitating vehicle with applied forces.

Here and in the following, the following notational conventions are used. Bold lowercase letters indicate vectors, while bold uppercase letters indicate matrices or tensors. Also, the notation $(\cdot)^{\mathcal{A}}$ denotes components in the generic \mathcal{A} triad. If \mathbf{R} is the rotation tensor that brings triad \mathcal{I} into triad \mathcal{B} , then the components of a generic vector \mathbf{a} in the two triads are related as $\mathbf{a}^{\mathcal{I}} = \mathbf{R}^{\mathcal{I}} \mathbf{a}^{\mathcal{B}}$. Furthermore, \mathbf{a}_{\times} is the skew-symmetric tensor associated with \mathbf{a} . Finally, the symbol $(\dot{\cdot}) = d \cdot / dt$ indicates derivation with respect to time.

The forces \mathbf{s}_T and \mathbf{s}_I in figure 4 represent the thrust and the interaction forces between the tail and the cavity respectively, \mathbf{s}_G is the weight of the projectile acting at the center of gravity of the vehicle while letters T , G and N respectively refer to the tail, the center of gravity and the nose of the vehicle. Also, δ_N and δ_{F_i} are the control deflection angles of the disc cavitator and the fins respectively.

The cavitator is the device at the nose that generates a cavity around the torpedo. Several cavitator geometries have been investigated by May [19]. We use a circular disc cavitator 0.07m in diameter which is typical for vehicles of the type being considered in this

study. The cavitator in this model is assumed to have only one degree of freedom about an axis in the horizontal plane, perpendicular to the longitudinal axis of the torpedo. The size and geometry of the cavity is a nonlinear function of the cavitator pitch angle and the direction of the velocity vector at the nose of the torpedo. Further, the wetted area of the fins and the torpedo depend on these angles which in turn determines the effectiveness of the fins.

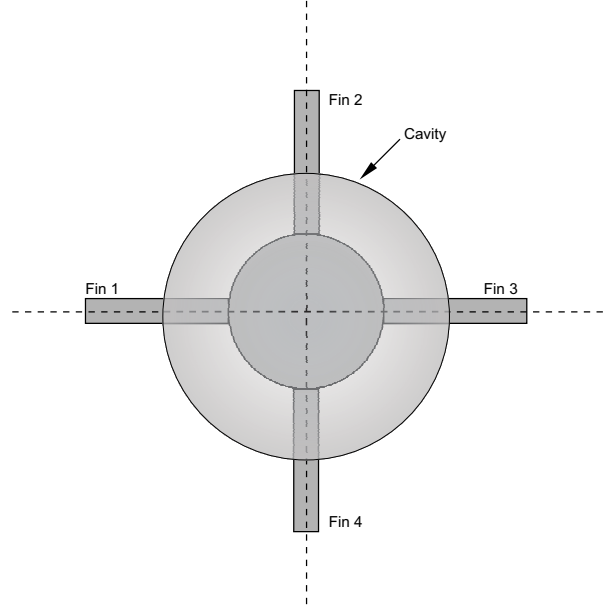


Figure 5: View of cruciform arrangement of fins (view from behind the vehicle)

The fins at the aft of the torpedo are essential to provide sufficient forces (shown in figure 4 as s_F) and moments for stability and control. The fins counteract the moments produced by the cavitator and provide the remaining lifting force required to balance the weight of the vehicle. A cruciform fin arrangement is considered, with all four fins being placed symmetrically along the girth of the torpedo near the tail (figure 5). In this work we assume that the horizontal fins can deflect independently of each other, and the differential fin deflections can give rise to control moments. Further, we assume the vertical fin deflections are equal in magnitude and opposite in direction. This serves to reduce the number of unknown controls in the system. Fins 1 and 3 are oriented parallel to the axis of rotation of the cavitator and are used as elevators to control the longitudinal dynamics

Table 1: Dimensions of torpedo.

Length	4.0m
Diameter	0.2m
Cavitator diameter	0.07m
Mass	150kg
Fin location	3.5m aft of nose
Fin sweepback angle	0 deg.

of the torpedo and stabilize it in pitch. The other two fins are the rudders used to control the lateral dynamics of the torpedo and stabilize it in roll. The fins are located 3.5m aft of the cavitator. Symmetric wedge shaped fins are chosen as they provide good strength characteristics and for small wedge angles, the transition between partial cavitation and supercavitation are confined to a very limited range of deflection angles [14].

The torpedo itself is 4.0m in length and 0.2m in diameter. Although the mass of the torpedo would change as the fuel for the propulsion system is consumed and ventilation gases are expelled, it is assumed constant at 150kg for the purposes of this analysis.

2.3 Equations of motion

The equations of motion are conveniently formulated in a body-fixed reference frame $\mathcal{F}_{P,\mathcal{B}}$, with origin in P and triad $\mathcal{B} = (\mathbf{b}_1, \mathbf{b}_2, \mathbf{b}_3)$. A reference inertial frame $\mathcal{F}_{O,\mathcal{I}}$ is centered at point O and has a triad of unit vectors $\mathcal{I} = (\mathbf{i}_1, \mathbf{i}_2, \mathbf{i}_3)$, as shown in figure 6. The equations of balance of linear and angular momentum (Euler's equations) of the vehicle expressed in terms of body-attached components can be expressed as

$$\dot{\mathbf{l}}^{\mathcal{B}} + \boldsymbol{\omega}^{\mathcal{B}} \times \mathbf{l}^{\mathcal{B}} = \mathbf{s}^{\mathcal{B}}, \quad (1)$$

$$\dot{\mathbf{h}}_P^{\mathcal{B}} + \mathbf{v}_P^{\mathcal{B}} \times \mathbf{l}^{\mathcal{B}} + \boldsymbol{\omega}^{\mathcal{B}} \times \mathbf{h}_P^{\mathcal{B}} = \mathbf{m}_P^{\mathcal{B}}, \quad (2)$$

where the linear momentum is $\mathbf{l} = m\mathbf{v}_P + \mathbf{S}_P^T \boldsymbol{\omega}$ and the angular momentum is given by $\mathbf{h}_P = \mathbf{S}_P \mathbf{v}_P + \mathbf{J}_P \boldsymbol{\omega}$. Letting ρ_V be the vehicle density, $m = \int_V \rho_V dV$ is the mass of the vehicle, $\mathbf{S}_P = \int_V \rho_V \mathbf{r} \times dV$ is the first moment of inertia, $\mathbf{J}_P = -\int_V \rho_V \mathbf{r} \times \mathbf{r} \times dV$ is the inertia dyadic, \mathbf{v}_P and $\boldsymbol{\omega}$ denote the linear velocity of point P and the angular velocity of the body, respectively, while \mathbf{s} and \mathbf{m}_P are the resultants of the applied forces and moments,

respectively.

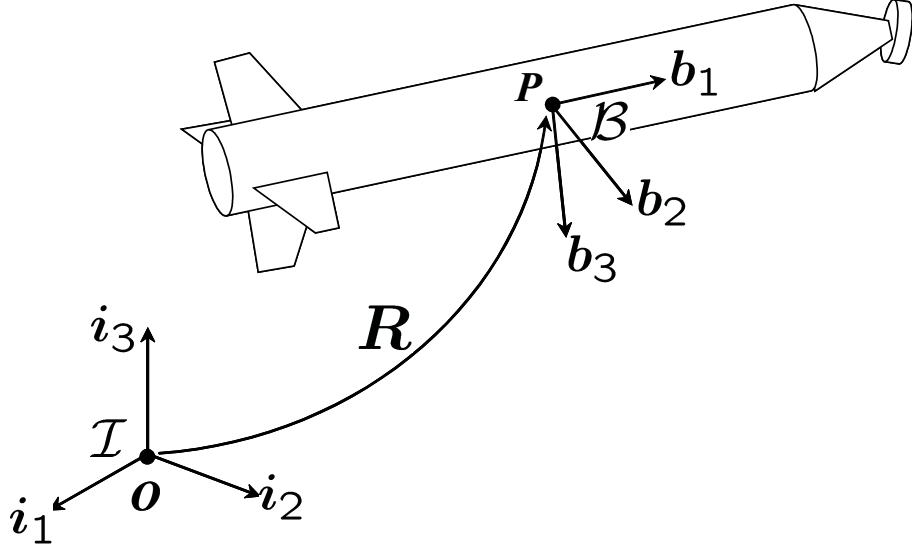


Figure 6: Body-fixed and inertial frames.

Equations (1,2) can be conveniently rewritten in the following compact form:

$$M^B \dot{\mathbf{w}}^B + \mathbf{w}^B \times M^B \mathbf{w}^B = \mathbf{f}^B, \quad (3)$$

where the generalized inertia tensor is defined as

$$M = \begin{bmatrix} m\mathbf{I} & \mathbf{S}_P^T \\ \mathbf{S}_P & \mathbf{J}_P \end{bmatrix}, \quad (4)$$

and where the generalized velocity \mathbf{w} and generalized force \mathbf{f} are defined as

$$\mathbf{w} = (\mathbf{v}_P^T, \boldsymbol{\omega}^T)^T, \quad \mathbf{f} = (\mathbf{s}^T, \mathbf{m}_P^T)^T. \quad (5)$$

In Eq. (3), $(\cdot) \times$ is the South-West cross product operator [4]:

$$\mathbf{w} \times = \begin{bmatrix} \boldsymbol{\omega} \times & \mathbf{0} \\ \mathbf{v}_{P \times} & \boldsymbol{\omega} \times \end{bmatrix}. \quad (6)$$

The position and orientation of the vehicle with respect to the inertial frame can be expressed through the position vector $\mathbf{u}_P = (P - O)$ and a set of rotation parameters, more specifically quaternions for this work. The vehicle kinematic equations can be written as

$$\dot{\mathbf{d}} = \begin{bmatrix} \mathbf{R}^I & \mathbf{0} \\ \mathbf{0} & \mathbf{E} \end{bmatrix} \dot{\mathbf{w}}^B, \quad (7)$$

where \mathbf{d} is the vector of the generalized coordinates defined as

$$\mathbf{d} = (\mathbf{u}_P^T, \mathbf{q}_4^T)^T, \quad (8)$$

with $\mathbf{q}_4 = (q_0, \mathbf{q}^T)^T$ denoting the quaternion vector. Also in Eq. (7), \mathbf{E} relates the time rates of the rotation parameters with the body-frame components of the angular velocity and is defined as:

$$\mathbf{E} = \frac{1}{2} \begin{bmatrix} -\mathbf{q}^T \\ q_0 \mathbf{I} + \mathbf{q}_\times \end{bmatrix}. \quad (9)$$

Equation (7) implicitly enforces the derivative of the unit quaternion condition, which can be expressed as:

$$\dot{\mathbf{q}}_4 \cdot \mathbf{q}_4 = 0. \quad (10)$$

2.4 Forces

The body is acted upon by a system of forces and moments corresponding to the interaction of the vehicle's control surfaces with the cavity boundaries. The control surfaces include the fins at the aft of the torpedo and the cavitator. The vehicle's motion is sustained by a propulsion force directed along the body axis.

The resultant \mathbf{s} of the forces acting on the vehicle can be written as

$$\mathbf{s} = \mathbf{s}_T + \mathbf{s}_N + \sum_{i=1}^{n_F} \mathbf{s}_{F_i} + \mathbf{s}_I + \mathbf{s}_G, \quad (11)$$

where $\mathbf{s}_T = \delta_T \mathbf{b}_1$ is the propulsive thrust, \mathbf{s}_N is the hydrodynamic force at the vehicle nose generated by the cavitator, \mathbf{s}_{F_i} are the hydrodynamic forces generated by the n_F fins, \mathbf{s}_I are the contact forces due to the interaction of the vehicle with the cavity, and finally $\mathbf{s}_G = -mg\mathbf{i}_3$ is the gravitational force. Similarly, the moments \mathbf{m}_P can be written as

$$\mathbf{m}_P = \mathbf{r}_{PT} \times \mathbf{s}_T + \mathbf{r}_{PN} \times \mathbf{s}_N + \sum_{i=1}^{n_F} \mathbf{r}_{PF_i} \times \mathbf{s}_{F_i} + \mathbf{r}_{PI} \times \mathbf{s}_I + \mathbf{m}_I + \mathbf{r}_{PG} \times \mathbf{s}_G, \quad (12)$$

where \mathbf{r}_{AB} indicates a distance vector from point A to point B , and T is the point of application of the thrust, N is the cavitator location, F_i is the aerodynamic center of the i th fin, I is the tail-cavity contact point, \mathbf{m}_I is the additional moment due to interaction of the vehicle with the cavity and finally G is the center of gravity.

2.4.1 Cavity shape and dimensions

The behavior of the cavity affects the forces at the nose of the vehicle and the immersion of the fins in the fluid, and the planing contact forces between vehicle and cavity boundary. An approximate, simplified model for the cavity is considered here. The model estimates cavity length, maximum diameter and shape for a given diameter of a circular, flat cavitator disk. In a cylindrical polar coordinate system, the nominal axisymmetric shape of the cavity is approximated using the formulation given by Munzer and Reichardt [21]:

$$r_c(x) = \frac{d_{\max}}{2} \left[1 - \left(\frac{x/d_c - l_c/2d_c}{l_c/2d_c} \right)^2 \right]^{1/2.4} \quad (13)$$

where $r_c(x)$ is the cavity radius at location x , while d_{\max} and l_c denote maximum diameter and length of the cavity, respectively given by:

$$d_{\max} = d_c \sqrt{\frac{C_D(\sigma, 0)}{\sigma}} \quad (14)$$

$$l_c = d_c \sqrt{\frac{C_D(\sigma, 0)}{\sigma^2} \ln\left(\frac{1}{\sigma}\right)} \quad (15)$$

In equations 94 and 95, d_c is the cavitator diameter, $C_D(\sigma, 0)$ is the cavitator drag coefficient and σ is the cavitation number, defined as:

$$\sigma = \frac{p_\infty - p_c}{1/2\rho v^2} \quad (16)$$

where p_∞, p_c are respectively the ambient and cavity pressures, v is the vehicles velocity and ρ is the fluid density. The cavitation number is a measure of the tendency of cavitation to occur in a flow and as such, it is a principal quantity governing cavity dimensions. The expression of the cavity shape defined by equation 93 ignores distortions due to turning and/or gravity and those associated with the cavitator's lift. It is also assumed that the cavity axis is aligned with the velocity of the cavitator. The significant cavity dimensions are shown in figure 7.

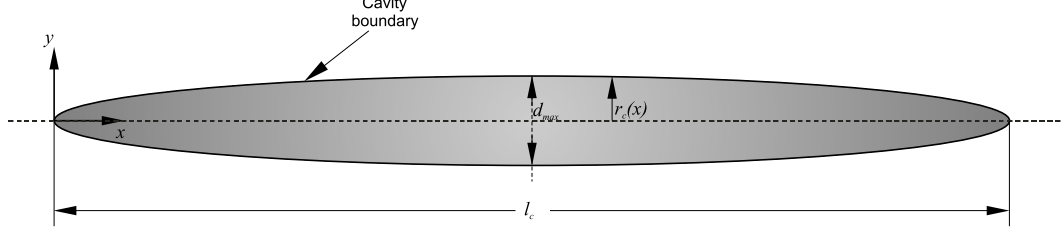


Figure 7: Cavity dimensions calculated using Reichardt formulation.

2.4.2 Nose-water interactions

The secondary function of the cavitator is to provide a lift force, which is obtained by orienting the cavitator at an appropriate angle. The achievement of optimal orientation of the cavity with respect to the vehicle during turning maneuvers requires this angle to be variable and controlled. The angle of attack α_C of the cavitator is defined as the angle between the velocity of the nose and a vector perpendicular to the nose surface. The angle of attack can be calculated in terms of the orientation of the cavitator with respect to the vehicle's axis which is denoted as δ_C . This angle can be controlled to modify the angle of attack seen by the cavitator and correspondingly, the force generated on the cavitator through its interaction with water can be used for controlling the vehicle by orienting the cavitator at an appropriate angle. The achievement of optimal orientation of the cavity with respect to the vehicle during turning maneuvers requires this angle to be controllable.

The hydrodynamic forces acting on a circular cavitator can be conveniently expressed in terms of a reference frame $\mathcal{F}_{N,N}$ located at the cavitator center N and with triad of unit vectors $\mathcal{N} = (\mathbf{n}_1, \mathbf{n}_2, \mathbf{n}_3)$. Unit vector \mathbf{n}_1 is perpendicular to the disk surface. Its orientation with respect to the vehicle axis \mathbf{b}_1 is defined by the control angle δ_N , so that the components of \mathbf{n}_1 in the body-fixed triad \mathcal{B} , labelled $\mathbf{n}_1^{\mathcal{B}}$, are

$$\mathbf{n}_1^{\mathcal{B}} = (\cos \delta_N, 0, -\sin \delta_N)^T. \quad (17)$$

Unit vector \mathbf{n}_2 is orthogonal to the plane formed by the pair of vectors \mathbf{v}_N and \mathbf{n}_1 , i.e.

$$\mathbf{n}_2 = \frac{\mathbf{v}_N \times \mathbf{n}_1}{\|\mathbf{v}_N \times \mathbf{n}_1\|}, \quad (18)$$

where $\mathbf{v}_N = \mathbf{v}_P + \boldsymbol{\omega} \times \mathbf{r}_{PN}$ is the cavitator velocity, \mathbf{r}_{PN} being the distance vector between

the reference point P on the vehicle and the cavitator center N . Finally, unit vector \mathbf{n}_3 completes a right handed triad: $\mathbf{n}_3 = \mathbf{n}_1 \times \mathbf{n}_2$. The components of the three unit vectors \mathbf{n}_1 , \mathbf{n}_2 and \mathbf{n}_3 measured in the body-attached triad \mathcal{B} readily give the components in \mathcal{B} of the rotation tensor $\mathbf{R}_{\mathcal{B} \rightarrow \mathcal{N}}$ that rotates the \mathcal{B} triad into the \mathcal{N} triad:

$$\mathbf{R}_{\mathcal{B} \rightarrow \mathcal{N}}^{\mathcal{B}} = [\mathbf{n}_1^{\mathcal{B}} | \mathbf{n}_2^{\mathcal{B}} | \mathbf{n}_3^{\mathcal{B}}]. \quad (19)$$

Hence, if $\mathbf{v}_N^{\mathcal{B}}$ denotes the components of the cavitator velocity in the \mathcal{B} triad, the components of the same vector in the cavitator triad \mathcal{N} are

$$\mathbf{v}_N^{\mathcal{N}} = \mathbf{R}_{\mathcal{B} \rightarrow \mathcal{N}}^{\mathcal{B}T} \mathbf{v}_N^{\mathcal{B}} = (u_N^{\mathcal{N}}, 0, w_N^{\mathcal{N}})^T. \quad (20)$$

The cavitator angle of attack α_N is measured in the \mathbf{v}_N , \mathbf{n}_1 plane (see figure 8), and it is computed as

$$\tan \alpha_N = \frac{w_N^{\mathcal{N}}}{u_N^{\mathcal{N}}}. \quad (21)$$

In the \mathbf{v}_N , \mathbf{n}_1 plane, the hydrodynamic force acting on the cavitator can be decomposed into lift and drag components, which can be computed as [14]

$$L_N = \frac{1}{2} \rho v_N^2 A_N C_D(\sigma, 0) \sin \alpha_N \cos \alpha_N, \quad (22)$$

$$D_N = \frac{1}{2} \rho v_N^2 A_N C_D(\sigma, 0) \cos^2 \alpha_N, \quad (23)$$

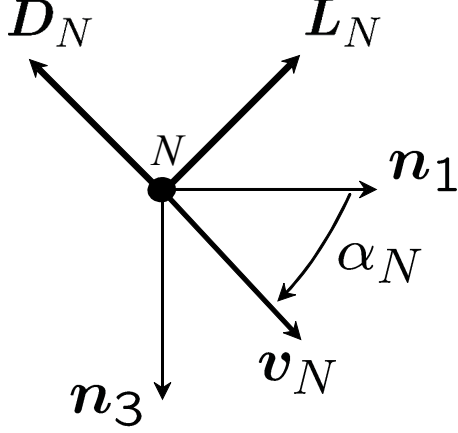
where A_N is the cavitator area. The hydrodynamic force can hence be expressed in the \mathcal{N} triad as

$$\mathbf{s}_N^{\mathcal{N}} = (L_N \sin \alpha_N - D_N \cos \alpha_N, 0, -L_N \cos \alpha_N - D_N \sin \alpha_N)^T, \quad (24)$$

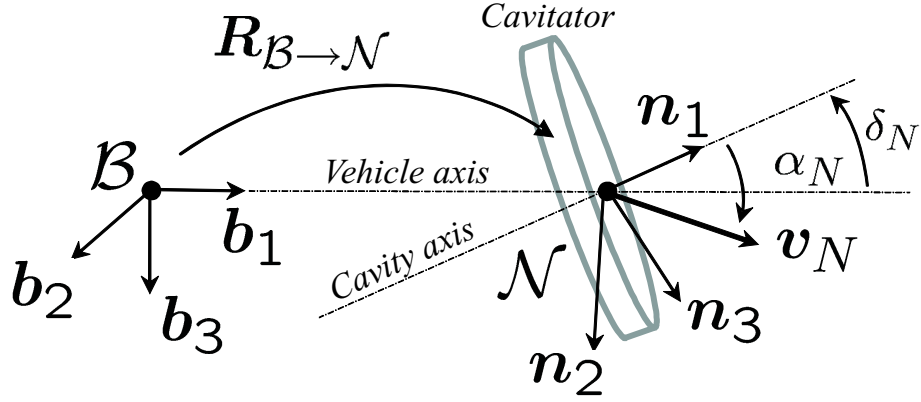
and transformed to the \mathcal{B} triad as $\mathbf{s}_N^{\mathcal{B}} = \mathbf{R}_{\mathcal{B} \rightarrow \mathcal{N}}^{\mathcal{B}} \mathbf{s}_N^{\mathcal{N}}$.

2.4.3 Fin Forces

The fins are controlled to provide lift in the after-body section and to maneuver the vehicle. We consider the 4-fin configuration shown in figure 4. Each fin interacts with the surrounding fluid with forces that depend on the immersion depth in the fluid, the velocity at the fin location with respect to the fluid, the fin geometry and the angle of attack.



(a) Lift and drag components in the v_N , n_1 plane.



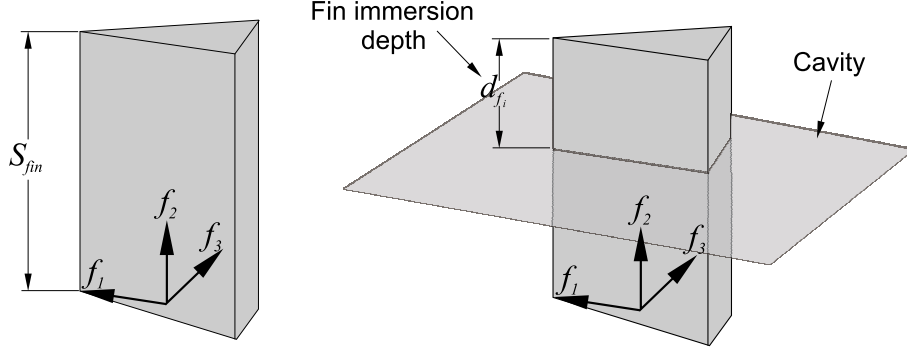
(b) Detail of cavitator.

Figure 8: Cavitator reference frame.

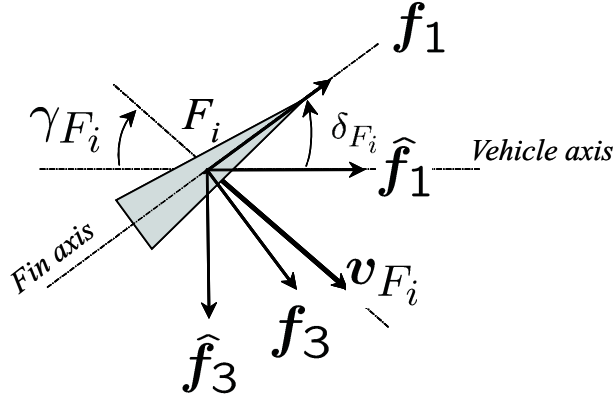
For convenience, the forces are first expressed in a reference frame $\mathcal{F}_{F_i, \mathcal{F}_i}$, with origin F_i and triad $\mathcal{F}_i = (\mathbf{f}_1, \mathbf{f}_2, \mathbf{f}_3)$ fixed to the i th fin, as shown in figure 9. Triad \mathcal{F}_i is obtained by a rotation that first brings \mathcal{B} into the undeflected fin configuration $\hat{\mathcal{F}}_i = (\hat{\mathbf{f}}_1, \hat{\mathbf{f}}_2, \hat{\mathbf{f}}_3)$, $\hat{\mathbf{f}}_k = \hat{\mathbf{R}}_i \mathbf{b}_k$, $k = 1, 2, 3$, followed by a rotation that accounts for the fin deflection δ_{F_i} , $\mathbf{f}_k = \mathbf{R}(\delta_{F_i}, \hat{\mathbf{f}}_2) \hat{\mathbf{f}}_k$, $k = 1, 2, 3$. The total rotation from \mathcal{B} to \mathcal{F}_i is hence $\mathbf{f}_k = \mathbf{R}_{\mathcal{B} \rightarrow \mathcal{F}_i} \mathbf{b}_k$, $\mathbf{R}_{\mathcal{B} \rightarrow \mathcal{F}_i} = \mathbf{R}(\delta_{F_i}, \hat{\mathbf{f}}_2) \hat{\mathbf{R}}_i$.

In the fin-fixed reference system, the forces are determined in terms of the angle of attack and of the immersion depth, according to results for wedge-shaped fins previously published [14]. The i th fin force components in \mathcal{F}_i ($i = 1, \dots, 4$) are given by

$$\mathbf{s}_{F_i}^{\mathcal{F}_i} = \frac{1}{2} \rho v_{F_i}^2 S (C_x(\gamma_{F_i}, d_{F_i}), C_y(\gamma_{F_i}, d_{F_i}), C_z(\gamma_{F_i}, d_{F_i}))^T, \quad (25)$$



(a) Detail of fin.



(b) Fin-fixed frame and fin velocity.

Figure 9: Fin reference frame and angle of attack.

where v_{F_i} is the magnitude of the velocity vector at the fin frame origin F_i , S is the fin surface and C_x, C_y, C_z are force coefficients defined in terms of the fin angle of attack γ_{F_i} and of the penetration distance d_{F_i} . The fin angle of attack in the local \mathcal{F}_i triad is obtained from the components of the velocity $\mathbf{v}_{F_i}^{\mathcal{F}_i} = (v_x, v_y, v_z)^T$. Accordingly, we have

$$\tan \gamma_{F_i} = \frac{v_z}{v_x}. \quad (26)$$

The fin force components are transformed from the \mathcal{F}_i to the body-fixed triad \mathcal{B} as $\mathbf{s}_{F_i}^{\mathcal{B}} = \mathbf{R}_{\mathcal{B} \rightarrow \mathcal{F}_i}^{\mathcal{B}} \mathbf{s}_{F_i}^{\mathcal{F}_i}$. Plots of the force coefficients are shown in figure 10. Their approximately bilinear behavior for assigned penetration depth is associated to two different flow regimes developing on the fin. The first flow regime occurs for low angles of attack, when two separate cavities are formed at the base and at the leading edge of the fin. For larger angles of attack the two cavities merge to form a supercavity that envelopes all the surfaces except for the pressure face. These forces were calculated using a fully three-dimensional

boundary-element method supplemented with a viscous drag correction [14]. Note that the bilinearity may cause problems in optimization due to sudden change of gradients, and to account for this, future efforts would be aimed at approximating this sharp change by a spline interpolation.

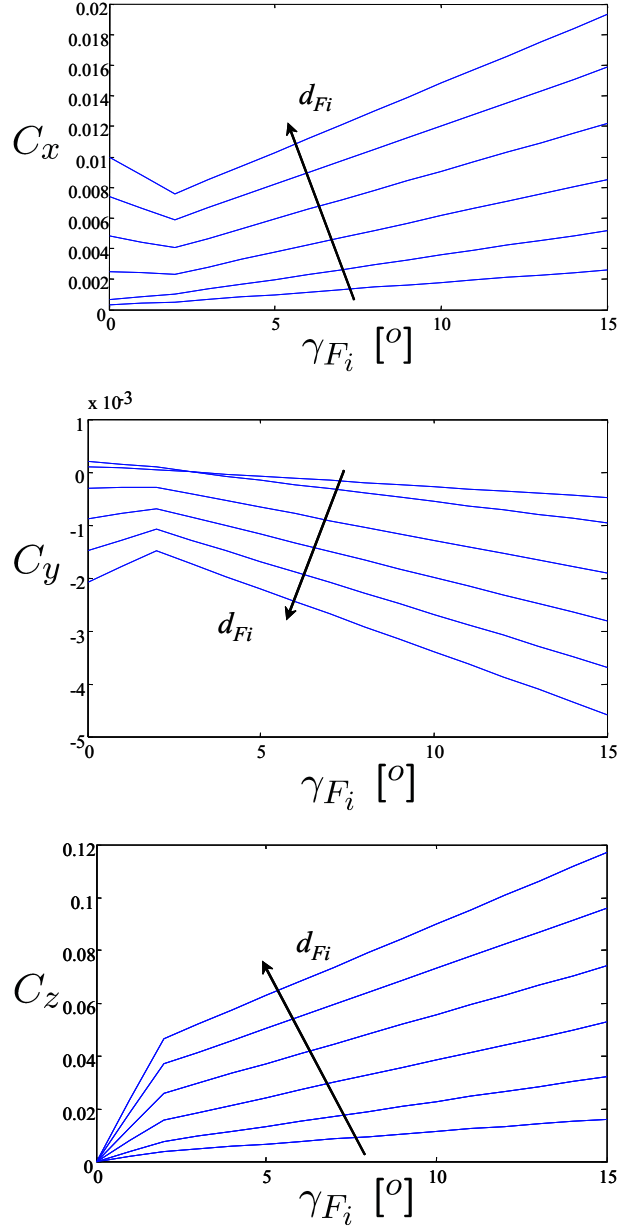


Figure 10: Fin force coefficients versus angle of attack, for varying penetration depth.

The angle of attack for the i th fin is given by:

$$\alpha_{Fi} = \gamma_{Fi} + \delta_{Fi} \quad (27)$$

where γ_{Fi} defines the orientation of the fin with respect to its velocity, while δ_{Fi} is the controlled fin deflection. The fin orientation is obtained from the components of the velocity in the fin-fixed reference frame which is given by:

$$\tilde{\mathbf{v}}_{Fi} = v_x \tilde{\mathbf{i}} + v_y \tilde{\mathbf{j}} + v_z \tilde{\mathbf{k}} = \mathbf{R}_{Fi}^T \bar{\mathbf{v}}_{Fi} \quad (28)$$

where $\bar{\mathbf{v}}_{Fi} = \bar{\mathbf{v}} + \bar{\boldsymbol{\omega}} \times \bar{\mathbf{r}}_{Fi/G}$. Accordingly:

$$\tan \gamma_{Fi} = \frac{v_z}{v_x} \quad (29)$$

2.4.4 Penetration distance

The fin penetration distance d_{Fi} is calculated in terms of the dimensions of the cavity sustained by the vehicle velocity. The distance of the fin from the cavity axis is given by

$$d_{Ci} = \|\mathbf{r}_{NF_i}\| \sin \theta, \quad (30)$$

where θ is the angle between the cavity axis $\mathbf{t} = -\mathbf{v}_N / \|\mathbf{v}_N\|$ and the distance vector between the cavitator and the fin, \mathbf{r}_{NF_i} , which can be computed as

$$\cos \theta = \frac{\mathbf{r}_{NF_i} \cdot \mathbf{t}}{\|\mathbf{r}_{NF_i} \cdot \mathbf{t}\|}, \quad (31)$$

according to figure 11. The penetration distance of the i th fin can at this point be approximated as

$$d_{Fi} = d_{Ci} - r_C(\xi_0), \quad (32)$$

where $r_C(\xi_0)$ is the cavity radius at location $\xi_0 = \|\mathbf{r}_{NF_i}\| \cos \theta$.

2.4.5 Tail-cavity Interaction forces - Simplified Approach

A simplified model is now presented to describe the ‘‘tail-slap’’ interactions. The contacts are modelled as short duration impacts between the body and an elastic surface. The associated forces are applied at the tail of the body and are considered proportional to the

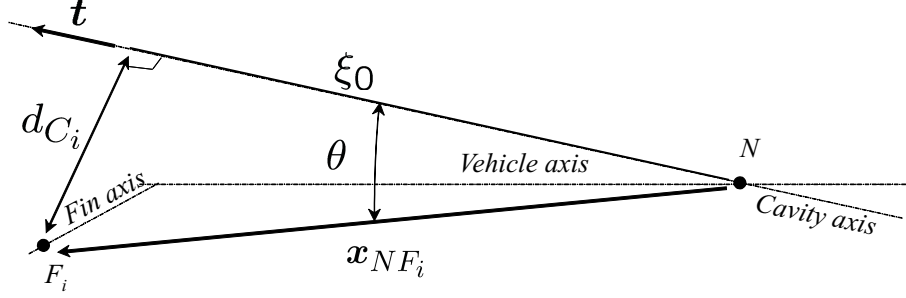


Figure 11: Calculation of fin penetration depth.

penetration distance d_T of the tail in the surrounding fluid. The penetration distance of the tail is calculated through a procedure similar to the one described for the fins. According to the assumptions here considered, the impact force can be described as

$$\mathbf{s}_I = K(d_T)d_T\mathbf{n}, \quad (33)$$

where \mathbf{n} is a unit vector perpendicular to the cavity axis at the impact location, pointing inward towards the cavity. The coefficient $K(d_T)$ is defined as

$$K(d_T) = \begin{cases} K_0 & \text{if } d_T \geq 0, \\ 0 & \text{if } d_T < 0, \end{cases} \quad (34)$$

and hence realizes a unilateral contact condition. The value of the equivalent stiffness K_0 in Eq. (34) is based upon experimental observations [19]. This model for the contact force is extremely simple, yet it is able to reproduce the interactions observed experimentally as described in Ref. [19].

2.4.6 Tail-cavity Interaction forces - Kulkarni and Pratap

Kulkarni and Pratap [15] have developed a tail-force model for phase 3 type interactions, i.e. intermittent tail-slaps. The impact force calculations are based on the concept that, during impact, the fluid motion occurs primarily in the transverse direction which is fixed in space and oriented normal to the vehicle axis. That is, the fluid flow is assumed occur in a plane normal to the axis of the vehicle and the flow components parallel to the vehicle axis are ignored (see figure 12). The motion of the fluid in each plane is considered to be

a 2-D phenomenon and independent of the flow exerted by any other flow plane over the entire wetted length.

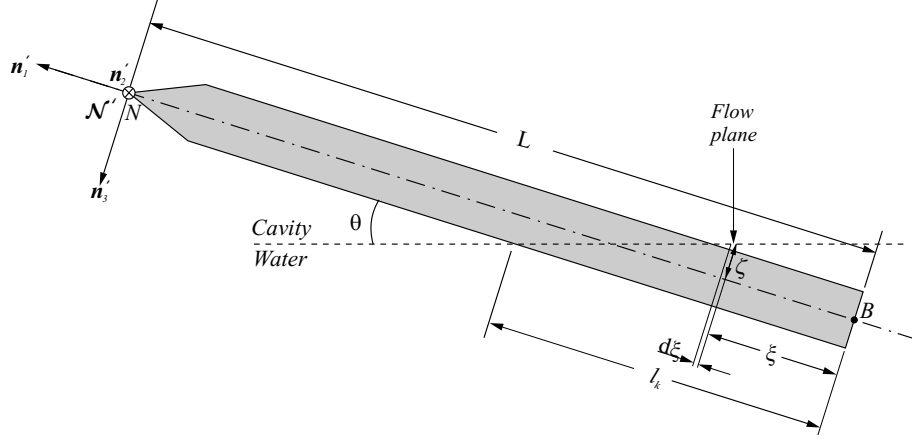


Figure 12: Impact force and moment calculation.

Figure 12 shows a schematic diagram (angle is exaggerated) of the projectile during impact with the cavity boundary. To describe the impact forces we introduce a nose-fixed reference frame $\mathcal{F}_{N,N'}$ with origin in Q and triad $\mathcal{N}' = (\mathbf{n}'_1, \mathbf{n}'_2, \mathbf{n}'_3)$. It has the same orientation as the body-fixed reference frame $\mathcal{F}_{P,B}$ described earlier. The angle at which the projectile impacts is denoted by θ . A new set of axes (ξ, ζ) is attached to the base of the projectile at point B. The ξ axis points in the same direction as the \mathbf{n}'_1 -axis while the ζ -axis points in the direction opposite to the \mathbf{n}'_1 -axis. The coordinate ξ denotes the distance between point B and any given fixed flow plane. The penetration into any such flow plane is given by ζ , which represents the distance from the projectile axis to the water surface in the flow plane. The wetted length of the projectile is denoted by l_k . The total force acting over the wetted length of the projectile is given by:

$$f_{imp} = -(K\rho d)(C_1 + C_2\dot{W} + C_3\dot{Q}) \quad (35)$$

where K is a constant that depends on the cross-section of the projectile. For circular cross section, $K = 2\pi$. Also, ρ is the density of water, d is the diameter of the projectile, and W is the component of translational velocity V at point A resolved along the Z_1 axis. Q is the angular velocity about the inertial axis Y_0 . The quantities C_1, C_2, C_3 are defined

as:

$$\begin{aligned}
C_1 &= W^2 l_k - Q^2 [(L - l_k)^3/3 - L^3/3] - 2WQ[(L - l_k)^2/2 - L^2/2] \\
C_2 &= (l_k^2/2) \tan \theta \\
C_3 &= [Ll_k^2 - l_k^2/2(L + l_k) + l_k^3/3] \tan \theta
\end{aligned} \tag{36}$$

L and l_k are defined as shown in figure 12. The moment exerted by this force about the center of mass of the vehicle is given by:

$$m_{imp} = -(K\rho d)(E_1 + E_2\dot{W} + E_3\dot{Q}) \tag{37}$$

where the quantities E_1, E_2, E_3 are defined as:

$$\begin{aligned}
E_1 &= W^2[l_k^2/2 - l_k x_{cm}] + 2WQ[l_k^2(L + x_{cm}) - l_k^3/3 - Lx_{cm}l_k] \\
&\quad \times Q^2[L^2l_k^2/2 - L^2x_{cm}l_k - 2Ll_k^3/3 + 2Lx_{cm}l_k^2/2 + l_k^4/4 - l_k^3x_{cm}/3] \\
E_2 &= [l_k^3/6 - l_k^2x_{cm}/2] \tan \theta \\
E_3 &= [l_k^3(L + x_{cm})/6 - l_k^4/12 - Lx_{cm}l_k^2/2] \tan \theta
\end{aligned} \tag{38}$$

where $x_{cm} = |\mathbf{r}_{TG}|$ is the norm of the distance vector from the center of gravity G to the tail T .

During impact, a drag force is generated at the tail of the projectile. The magnitude of this force depends on the depth of penetration of the tail and the angle the projectile makes with the cavity boundary. Figure 13 shows the cross section of the projectile at a distance ξ from point B. It is being viewed along the X_1 direction. The radius of the projectile is r and its diameter is d . The depth of penetration at this cross-section is ζ . The expressions for the component of this force in the X_1 -direction and Z_1 direction are as follows:

$$f_{X_1_{IMPD}} = -\frac{1}{2}\rho k U^2 \left[r^2 \cos^{-1} \left(\frac{r - l_k \tan \theta}{r} \right) - (r - l_k \tan \theta) \sqrt{d l_k \tan \theta} \right] \tag{39}$$

$$f_{Z_1_{IMPD}} = -\rho k \sqrt{d \tan \theta} f_1 \tag{40}$$

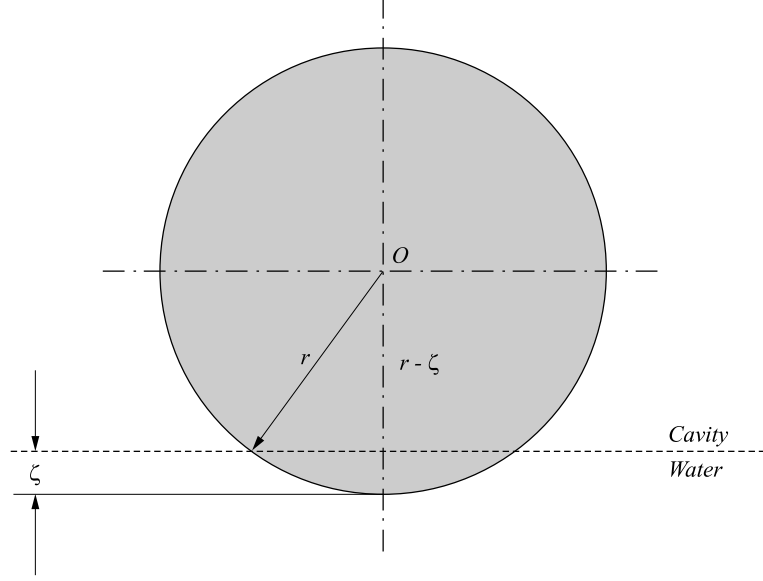


Figure 13: Partly immersed tail section.

where

$$f_1 = \frac{16}{105}Q^2l_k^{7/2} + \frac{2}{3}W^2l_k^{3/2} + \frac{4}{3}WQLl_k^{3/2} + \frac{2}{3}Q^2L^2l_k^{3/2} - \frac{8}{15}Ql_k^{5/2}(W - QL) \quad (41)$$

which is obtained by integrating the force acting on each flow plane over the wetted length of the vehicle to give the lift force acting on the vehicle due to after-body interaction with the cavity.

Finally, we write the total interaction force and moment as follows:

$$\begin{aligned} \mathbf{s}_I &= (f_{X_{1_{IMPD}}}, 0, f_{imp} + f_{Z_{1_{IMPD}}}) \\ \mathbf{m}_I &= (0, m_{imp}, 0) \end{aligned} \quad (42)$$

2.4.7 Tail-cavity Interaction forces - Hassan Theory

The operation of supercavitating vehicle dynamics can be broadly categorized into three distinct phases of motion as described in section 1.4; cavity-riding, planing and intermittent tail-slaps with the cavity. The latter two phases involve interaction of the tail section of the vehicle with the cavity, giving rise to certain interaction forces.

Hassan [11] presents a theory for forces and moments acting on the partially transom of supercavitating vehicles. This theory is rooted in Wagner's planing theory and discussed in detail in Logvinovich ([17], [18]). The basic theory with the addition of viscous corrections is presented first, followed by calculation of forces and centers of pressure for two special cases. These are: (1) circular cylinder planing on a flat surface and (2) circular cylinder planing on a curved surface.

The steady state planing forces and moments for immersion of a planar circular profile into a fluid are first calculated. The circular profile has a radius R submerged through a flat free surface till depth h (see figure 14).

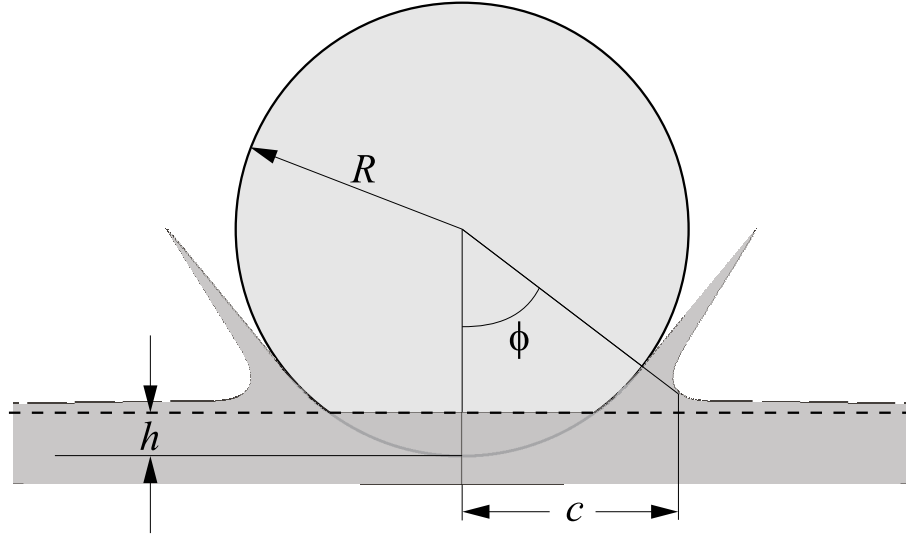


Figure 14: Immersion of the cylindrical profile in water.

The induced mass is denoted as m^* and M is the apparent induced mass, taking into account the non-holonomic dynamics associated with the spray sheet [11]. The net vertical force acting on the immersed part of the cylindrical profile and the net moment acting about the base of the cylinder (see figure 15) are given as:

$$F_p = \int_0^l \left\{ \frac{V_n^2}{\chi^2} \frac{\partial M}{\partial h} \right\} dx$$

$$M_p = - \int_0^l \left\{ x \frac{V_n^2}{\chi^2} \frac{\partial M}{\partial h} \right\} dx$$

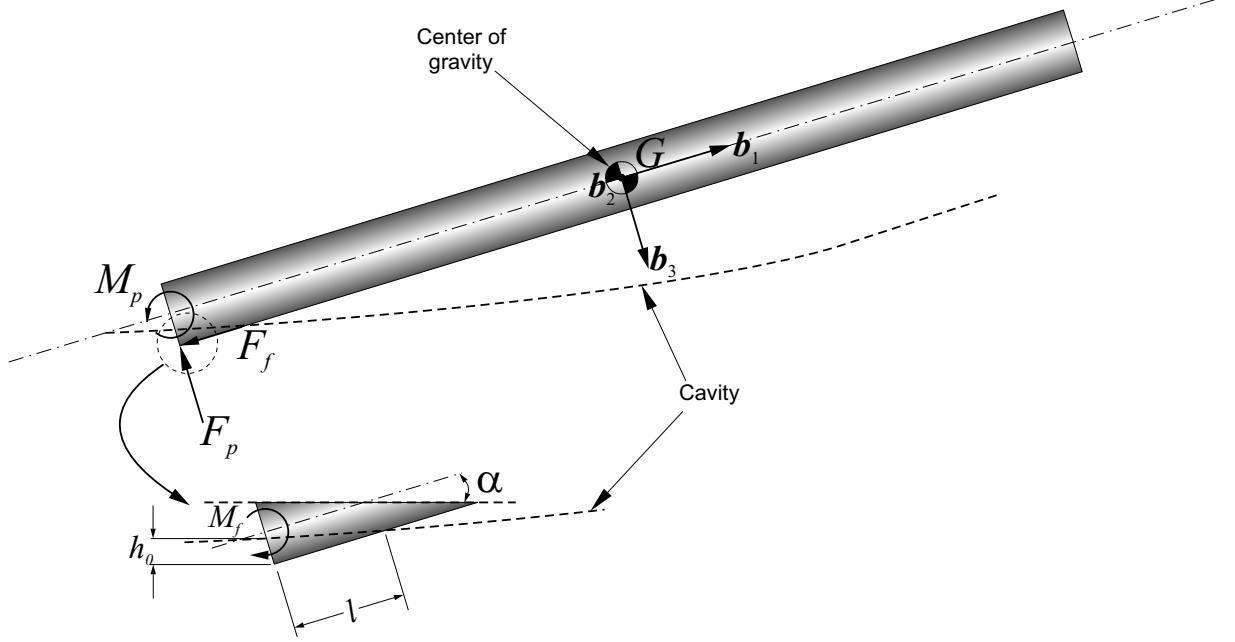


Figure 15: Planing of the cylinder on the cavity surface.

where V_n is the component of the free stream velocity normal to the longitudinal axis of the planing surface. Also, χ is called the transport parameter and it is defined as:

$$\chi = 1 - \frac{\tan \alpha}{2\rho c} \frac{\partial m^*}{\partial x}, \quad (43)$$

where ρ is the fluid density, α is the angle of attack of the vehicle and c is the lateral distance from the vertical axis to the spray sheet root as indicated in figures 14 and 15.

The net force acting over the wetted surface and the moment acting about the base of the cylinder, associated with viscous effects, that is, arising due to frictional forces, can be expressed as:

$$\begin{aligned} F_f &= 1/2\rho V^2 \cos^2 \alpha C_D S_w \\ M_f &= -\rho C_D V^2 \cos^2 \alpha R^2 \int_0^l \sin \phi(x) dx \end{aligned} \quad (44)$$

where S_w is the wetted surface area, V is the x component of velocity, the angle ϕ is defined as shown in figure 14 and C_D is the drag coefficient for a smooth plate, given as:

$$C_D = \frac{0.031}{Re_v^{1/7}} \quad (45)$$

Here Re_ν is the Reynolds number based on wetted longitudinal length of the planing surface.

For a circular cylinder of constant radius R , the wetted surface area is computed as:

$$S_w = 2R \int_0^l \phi(x) dx \quad (46)$$

The special case of a cylinder planing on a flat free surface is considered next. The relationships for the resulting forces and moments arising under this set of conditions are given below:

$$\begin{aligned} F_p &= 2\rho\pi V^2 R^2 \sin\alpha \cos\alpha \frac{h_0}{R} \left[1 - \frac{2}{3\pi} \sqrt{\frac{h_0}{R}} \left(\frac{4}{3} + \ln \left\{ 4\sqrt{\frac{R}{h_0}} \right\} \right) \right] \\ M_p &= 2\rho\pi V^2 R^2 l \sin\alpha \cos\alpha \frac{h_0}{R} \left[\frac{1}{2} - \frac{4}{15\pi} \sqrt{\frac{h_0}{R}} \left(\frac{24}{15} + \ln \left\{ 4\sqrt{\frac{R}{h_0}} \right\} \right) \right] \\ S_w &= \frac{8R^2}{3 \tan\alpha} \left(\frac{h}{R} \right)^{3/2} \left[1 + \frac{2}{5} \frac{h}{R} \right] \\ F_f &= -\frac{\rho}{2} V^2 \cos^2\alpha C_D \frac{R^2}{4 \tan\alpha} \left[\left(8 \left(\frac{h_0}{R} \right) - 1 \right) \arcsin \left(2\sqrt{\frac{h_0}{R}} \right) + 2\sqrt{\frac{h_0}{R}} \sqrt{1 - 4\frac{h_0}{R}} \right] \\ M_f &= -\frac{4}{3} \rho V^2 \cos^2\alpha C_D l R^2 \sqrt{\frac{h_0}{R}} \end{aligned} \quad (47)$$

Similarly the special case of a circular cylinder planing on a circular cylindrical free surface is considered. This configuration resembles closely the case of a vehicle planing on the cavity surface when the cavity radius is comparable to the radius of the vehicle.

$$\begin{aligned}
F_p &= \rho\pi R_0^2 V^2 \sin\alpha \cos\alpha \left(1 - \left\{\frac{\Delta}{h_0 + \Delta}\right\}^2\right) \left(\frac{R + h_0}{R + 2h_0}\right) \\
M_p &= \rho\pi R_0^2 V^2 \cos^2\alpha \left(1 - \left\{\frac{h_0^2}{h_0 + \Delta}\right\}\right) \left(\frac{R + h_0}{R + 2h_0}\right) \\
S_w &= \frac{R^2}{8\Delta \tan\alpha} \left(\begin{aligned} &2\left(R - \frac{8\Delta h_0}{R}\right) \arcsin\left\{\sqrt{1 - \frac{4\Delta h_0}{R^2}}\right\} - 32\Delta\sqrt{\Delta h_0} - \\ &16\frac{\Delta}{R}(2h_0 + \Delta) \arcsin\left\{\frac{\Delta + h_0}{\Delta - h_0}\right\} + \\ &4\sqrt{\Delta h_0}\sqrt{1 - \frac{4\Delta h_0}{R^2}} + 8\pi\frac{\Delta}{R}(2h_0 + \Delta) - R\pi \end{aligned} \right) \\
F_f &= \frac{1}{2}\rho V^2 \cos^2\alpha C_D S_w \\
M_f &= \frac{4}{3}\rho V^2 \cos^2\alpha C_D l \left(\begin{aligned} &3\frac{\Delta}{h_0} \tan^{-1}\left(\sqrt{\frac{h_0}{\Delta}}\right) (R^2 + 2R\Delta + 2\Delta^2) + \\ &(2\Delta + R)\sqrt{\Delta h_0} - 3\sqrt{\frac{\Delta}{h_0}}(R^2 + 2\Delta^2) - 6R\sqrt{\Delta}\frac{\Delta}{h_0} \end{aligned} \right) \\
&\quad \left(\frac{h_0\Delta}{R^2} \ll 1\right) \tag{48}
\end{aligned}$$

Finally, we write the total interaction force and moment due to planing in the body-fixed reference frame $\mathcal{F}_{P,B}$ as follows:

$$\begin{aligned}
\mathbf{s}_I &= (F_f, 0, F_p)^T \\
\mathbf{m}_I &= (0, M_p + M_f, 0)^T \tag{49}
\end{aligned}$$

We currently use the simplified model for calculation of planing forces. However, we intend to implement the Hassan model in the future because it is the most advanced of the three models presented thus far.

Chapter III

TRAJECTORY OPTIMIZATION

3.1 Overview

In this work we are interested in computing maneuvers of supercavitating vehicles. In the context of this thesis, computing a maneuver means determining the time histories of the vehicle controls and the associated time histories of vehicle states. Any computed maneuver must always satisfy a certain number of requirements, as detailed in the following.

First, maneuvers must be compatible with the vehicle dynamics, i.e. they must satisfy the equations of motion within the admissible limits imposed by the vehicle flight envelope and the necessarily limited control authority of the vehicle actuators. Clearly, this requirement is also relevant to the guidance and navigation problem. In fact, guiding a supercavitating vehicle along a compatible maneuver is accomplished more easily than when trajectories are specified upfront, for example through spline interpolation of given waypoints. Such strategies may in fact result into infeasible trajectories, especially if aggressive and high performance maneuvering is required.

Second, maneuvers should possibly be optimal in some sense, i.e. they should minimize some cost function, such as the time necessary to accomplish a given goal, or the final vehicle velocity, or yet again the control effort necessary to steer the vehicle. In fact, optimality provides a way to select one meaningful solution among the typically infinite possible different ways of achieving a same goal.

Finally, maneuvers must satisfy possible operational constraints imposed by the vehicle user in order to satisfy safety, cost, effectiveness and other needs.

3.2 Optimization Techniques

All the above mentioned requirements can be met by expressing each maneuver as the solution of an appropriate optimal control problem [9]. Generally speaking, the formulation

of an optimal control problem involves computation of the controls and states that minimize a certain cost function subject to the equations of state and possibly, additional problem-dependent constraints.

There are essentially two alternative strategies [3] for the solution of such optimal control problems. In the indirect approach, the optimal control equations are derived, i.e., the state, adjoint and control equations along with the transversality conditions (conditions imposed on the boundary values of the state variables or on the time boundaries themselves). This defines an infinite-dimensional non-linear multi-point boundary value problem. To solve this problem a suitable numerical method usually needs to be implemented in order to render the problem finite-dimensional.

In the direct approach one first discretizes the system dynamic equations (this is called direct transcription) and the associated states and controls using a suitable numerical method. The cost function, constraints and boundary conditions are then expressed in terms of the discrete values of states and controls. This results in a finite-dimensional non-linear programming problem. The discrete unknowns that include the discretized states and controls of the original infinite-dimensional problem are determined so as to minimize the scalar objective function while satisfying the constraints thus solving the optimal control problem.

The direct approach has some important advantages over the indirect method. First, the indirect method requires derivation of the optimal control equations, which can be a tedious task for complex systems. Secondly, in the indirect method, one needs to provide starting guesses for the system states as well as the adjoint variables. The adjoint variables in general might not have any physical meaning (unlike the system states) and therefore can be difficult to initialize. This is not the case in the direct approach where only the system states and controls need to be initialized, both of which have physical meaning. Finally, in the indirect approach one needs to define a-priori the constrained and unconstrained sub-arcs for problems with state inequalities, which then reduces the generality of the method. The direct approach avoids all these drawbacks and hence is the chosen method for solving out optimal control problem.

3.2.1 Direct and Indirect Methods: Single DOF Problem

In order to illustrate the difference between the direct and indirect methods we solve a simple single degree of freedom problem stated as follows [9]:

Given

$$\begin{aligned}
 \dot{v} &= a, \\
 \dot{x} &= v, \\
 v(0) &= -v(1) = 1, \\
 x(0) &= x(1) = 0,
 \end{aligned} \tag{50}$$

find $a(t)$ in $0 \leq t \leq 1$ to minimize

$$J = \frac{1}{2} \int_0^1 a^2 dt, \tag{51}$$

with the constraint that $x(t) \leq l$.

First we solve the problem by the indirect method. We consider $a(t)$ to be the control variable. The solution to the unconstrained problem, ($l \geq \frac{1}{4}$), is now obtained. The Euler-Lagrange equations are obtained as:

$$\begin{aligned}
 \dot{\lambda}_v &= -\lambda_x, \dot{\lambda}_x = 0, \dot{\lambda}_E = 0, \lambda_v = -\lambda_x t + const; \\
 \lambda_x &= const, \lambda_E = const = 1; a = -\lambda_v,
 \end{aligned} \tag{52}$$

where $\lambda_v, \lambda_x, \lambda_E$ are the Lagrange multipliers. The solution for this system is obtained as:

$$\begin{aligned}
 a = -2, v = 1 - 2t, x = t(1 - t) \Rightarrow (x)_{max} = \frac{1}{4}, \lambda_v = -a = 2, \lambda_x = 0, \\
 J = 2, H = \lambda_x \dot{x} + \lambda_v \dot{v} + \lambda_E \dot{E} = -2.
 \end{aligned} \tag{53}$$

The solution with constraint $\frac{1}{6} \leq l \leq \frac{1}{4}$ is obtained as follows:

$$a = \begin{cases} -8(1 - 3l) + 24(1 - 4l)t, & 0 \leq t \leq \frac{1}{2}, \\ -8(1 - 3l) + 24(1 - 4l)(1 - t), & \frac{1}{2} < t < 1; \end{cases}$$

$$v = \begin{cases} 1 - 8(1 - 3l)t + 12(1 - 4l)t^2, & 0 \leq t \leq \frac{1}{2}, \\ -1 + 8(1 - 3l)(1 - t) - 12(1 - 4l)(1 - t)^2, & \frac{1}{2} < t < 1; \end{cases}$$

$$x = \begin{cases} t - 4(1 - 3l)t^2 + 4(1 - 4l)t^2, & 0 \leq t \leq \frac{1}{2}, \\ 1 - t - 4(1 - 3l)(1 - t)^2 + 4(1 - 4l)(1 - t)^3, & \frac{1}{2} \leq t \leq 1; \end{cases}$$

$$\lambda_v = -a \rightarrow \lambda_v(\frac{1}{2}-) - \lambda_v(\frac{1}{2}+) = 0$$

$$\lambda_x = \begin{cases} 24(1 - 4l), & 0 \leq t \leq \frac{1}{2}, \\ -24(1 - 4l), & \frac{1}{2} \leq t \leq 1; \end{cases}$$

Also, we have

$$\lambda_x(\frac{1}{2}-) - \lambda_x(\frac{1}{2}+) = 48(1 - 4l), \quad (54)$$

$$J = 2 + 6(1 - 4l)^2, \quad (55)$$

$$H = -8(1 - 6l)^2. \quad (56)$$

We now solve the same problem by the direct method. We discretize the system of equations on a grid \mathcal{T}_h . This grid consists of n intervals t_0, t_1, \dots, t_n and $n + 1$ nodes p_0, p_1, \dots, p_{n+1} (see figure 16).

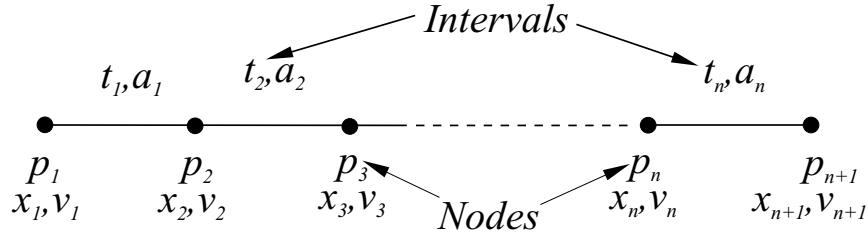


Figure 16: Nodes and intervals

The discretized system dynamics equations which are also the constraint equations for this problem can be written as follows,

$$\frac{v_i + v_{i+1}}{2} = \frac{x_{i+1} - x_i}{dt}, i = 1, \dots, n, \quad (57)$$

$$a_i = \frac{v_{i+1} - v_i}{dt}, i = 1, \dots, n. \quad (58)$$

The remaining constraints are written as,

$$v(1) = 1, v(n+1) = -1, \quad (59)$$

$$x(1) = 0, x(n+1) = 0. \quad (60)$$

Finally, the cost function is written in terms of the discretized variables as,

$$J = \frac{1}{2} \sum_{j=1}^n (a_j^2 dt) \quad (61)$$

In figure 17 we see that the optimized displacements calculated almost coincide with the analytical solution for displacement. Increasing the resolution of the grid has little effect on the displacements calculated.

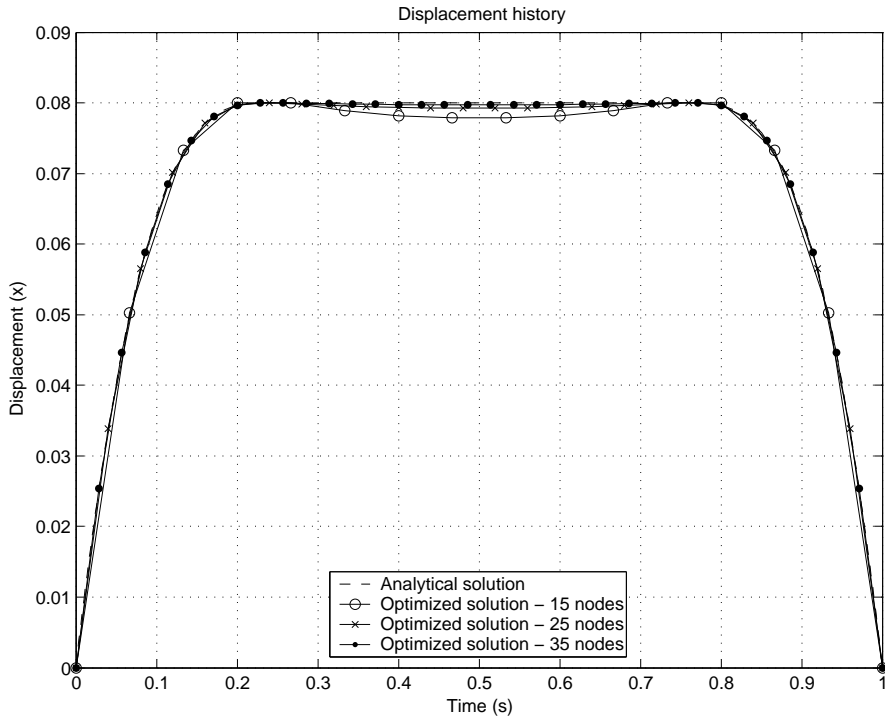


Figure 17: Optimized displacement and analytical solution

Finally, in figure 18 we see the error between the optimized trajectory and the analytically computed trajectory for increasing mesh density. We observe that the error in general reduces as the number of nodes used increases. The error e_i is calculated as:

$$e_i = \sum_{j=1}^{n_i} |x_{opt}(t_j) - x_{anal}(t_j)| \quad (62)$$

where n_i is the number of nodes in the i th grid, t_j is the time at the j th interval, and $x_{opt}(t_j)$ and $x_{anal}(t_j)$ are respectively the optimized and analytical displacements at time t_j .

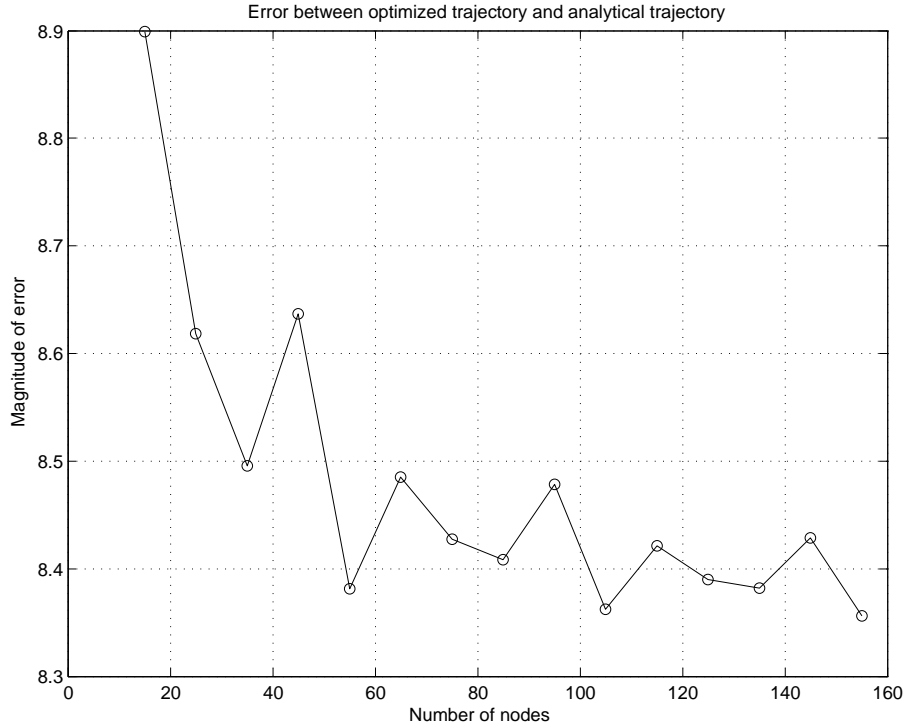


Figure 18: Magnitude of error vs. number of nodes used

From the above example we see that the direct method requires grid refinement in order to approach the analytical solution but does not require derivation of the optimal control equations [53]. These equations become very tedious to calculate as the number of variables and system complexity increases. Refining the grid in the direct method leads to rapid convergence to the analytical solution and simultaneously avoids the need to calculate the optimal control equations. For these reasons we choose to implement the direct method to solve our optimal control problem.

3.3 *The Optimal Control Problem For the Supercavitating Torpedo*

In order to formulate the problem and also describe the solution technique used for solving the optimal control problem for our system, let us introduce some notation. The problem domain is here noted $\Omega = (T_0, T) \subset \mathbb{R}$, and its boundary is $\Gamma = \{T_0, T\}$, $t \in \Omega$, where the final time T is possibly unknown. The dynamic equations of a rigid supercavitating vehicle introduced in the previous section (eqn. 3) and the kinematic equations (eqn. 7) are for convenience rewritten in compact form as:

$$\dot{\mathbf{y}} - \mathbf{z}(\mathbf{y}, \mathbf{u}) = 0, \quad (63)$$

where $\mathbf{y} \in \mathbb{R}^{n_y}$ denotes the vehicles states, $\mathbf{y} = (\mathbf{v}_P, \boldsymbol{\omega}, \mathbf{u}_P, \mathbf{q}_4)^T$, $n_y = 13$, while the controls $\mathbf{u} \in \mathbb{R}^{n_u}$ are $\mathbf{u} = (\delta_T, \delta_N, \delta_{F_1}, \delta_{F_2}, \delta_{F_3}, -\delta_{F_2})^T$, $n_u = 6$, and include the propulsion force δ_T , the cavitator angle δ_N , and the fin deflections δ_{F_i} , ($i = 1, 2, 3$). Note that fins 1 and 4 act as a rudder and deflect of the same amount, so that in reality there are only 5 independent controls. Also in Eq. (63), $\mathbf{z}(\mathbf{y}, \mathbf{u})$ is as given in the previous sections.

The optimal vehicle state time histories $\mathbf{y}_{\text{opt}}(t)$ and associated control policy $\mathbf{u}_{\text{opt}}(t)$ define an optimal maneuver and minimize the cost function

$$J = \phi(\mathbf{y}, \mathbf{u}, t)|_{\Gamma} + \int_{\Omega} L(\mathbf{y}, \mathbf{u}, t) dt. \quad (64)$$

As previously stated, the optimal solution must satisfy the vehicle equations of motion (Eq. (63)), which can therefore be interpreted as constraints of the optimization problem. Constraints on the states and the controls further characterize and define the maneuver, for example by providing initial and final conditions, or by providing operational and flight envelope limits. For generality, all these conditions can be expressed as inequality constraints in the form $x \in [x_{\min}, x_{\max}]$, i.e. $x_{\min} \leq x \leq x_{\max}$. Equality constraints are enforced by simply selecting $x_{\min} = x_{\max}$. The initial and terminal state conditions can be written as:

$$\boldsymbol{\psi}(\mathbf{y}(T_0)) \in [\boldsymbol{\psi}_{0_{\min}}, \boldsymbol{\psi}_{0_{\max}}], \quad (65)$$

$$\boldsymbol{\psi}(\mathbf{y}(T)) \in [\boldsymbol{\psi}_{T_{\min}}, \boldsymbol{\psi}_{T_{\max}}], \quad (66)$$

while non-linear constraints on states and controls can be expressed in general as

$$\mathbf{g}(\mathbf{y}, \mathbf{u}, t) \in [\mathbf{g}_{\min}, \mathbf{g}_{\max}]; \quad (67)$$

similarly, constraints at a (possibly unknown) internal event T_i are

$$\mathbf{g}(\mathbf{y}, \mathbf{u}, T_i) \in [\mathbf{g}_{T_i_{\min}}, \mathbf{g}_{T_i_{\max}}]; \quad (68)$$

integral conditions on states and controls can be given as

$$\int_{\Omega} \mathbf{h}(\mathbf{y}, \mathbf{u}, t) dt \in [\mathbf{h}_{\min}, \mathbf{h}_{\max}], \quad (69)$$

and finally upper and lower bounds are

$$\mathbf{y} \in [\mathbf{y}_{\min}, \mathbf{y}_{\max}], \quad (70)$$

$$\mathbf{u} \in [\mathbf{u}_{\min}, \mathbf{u}_{\max}]. \quad (71)$$

According to Optimal Control Theory, an optimal solution to this problem is determined by first defining an augmented performance index, obtained by adjoining the system governing equations (63) and constraints (65–69) to the performance index (64) through the use of Lagrange multipliers (co-states). Next, the stationarity of the augmented index is imposed, resulting in the definition of a set of differential equations in the states, co-states and controls, together with a set of associated boundary conditions[9].

3.4 Numerical Solution

This approach is however not convenient as described in earlier sections. We opt to avoid the derivation of the optimal control equations altogether by first discretizing the system equations (63) on a grid \mathcal{T}_h of the computational domain through some numerical discretization method. This defines the set of unknown parameters, represented by the discrete values of the states and controls on the computational grid, here noted $\mathbf{x} \in \mathbb{R}^{n_x}$. At this point,

the problem cost function (64) and the boundary conditions and constraints (65–69) are expressed in terms of the discrete parameters \mathbf{x} . This process defines a finite-dimensional Non-Linear Programming (NLP) problem, written as

$$\begin{aligned} \min_{\mathbf{x}} K(\mathbf{x}), \\ \text{s.t.: } \phi(\mathbf{x}) \in [\phi_{\min}, \phi_{\max}], \end{aligned} \tag{72}$$

where $\phi : \mathbb{R}^{n_x} \rightarrow \mathbb{R}^{n_\phi}$ are the optimization constraints, that include the discretized system dynamic equations, the discretized constraints and the boundary conditions. Here again, necessary conditions for a constrained optimum are obtained, similarly to the case of optimal control, by combining the objective K with the constraints through the use of Lagrange multipliers, and imposing the stationarity of the augmented cost function. The resulting large but sparse problem can be solved efficiently by Sequential Quadratic Programming (SQP) methods [1] or Interior Point (IP) methods [24].

The discretization of the equations of motion can in principle be based on any valid numerical method. For example, one may use a finite element method in the temporal domain in Ref. [6], or a non-linearly unconditionally stable energy preserving method in Ref. [5]. Many other valid choices are clearly possible. In this work, for simplicity we use the mid-point rule, which yields a second order solution. This method can also be interpreted as the lowest order member of the family of Discontinuous Petrov-Galerkin finite elements of [7].

To introduce the discretization of the equations, we consider a grid \mathcal{T}_h of $\overline{\Omega}$. In particular, we let the partition $T_0 \equiv t_0 < t_1 < \dots < t_{n-1} < t_n \equiv T$ be composed of $n \geq 1$ intervals $T^i = [t_i, t_{i+1}]$ of size h^i , $i = 0, \dots, n-1$. Since T is in general unknown, we introduce a mapping of time onto a fixed domain parameter s , i.e. $s : (T_0, T) \mapsto (0, 1)$, with the natural choice $s = t/(T - T_0)$, $s \in [0, 1]$. This yields the generic time step length as $h^i = (T - T_0)(s_{i+1} - s_i)$, $i = 0, \dots, n-1$, which is now expressed in terms of the step length in the s space and of the unknown maneuver duration.

The discretized system dynamics equations can be written on the generic interval T^i as

$$\mathbf{y}_{i+1} - \mathbf{y}_i - h^i \mathbf{z} \left(\frac{\mathbf{y}_i + \mathbf{y}_{i+1}}{2}, \mathbf{u}^i \right) = 0, \quad i = 1, \dots, n-1, \tag{73}$$

where $\mathbf{y}_i, \mathbf{y}_{i+1}$ are the values of the states at times t_i, t_{i+1} , respectively, and \mathbf{u}^i is the constant value of the controls within T^i . Note that, coherently with their algebraic nature, controls are treated as internal unknowns, which reflects the fact that no boundary conditions can be associated with these variables.

Given the discretization of the equations expressed by (73), the NLP variables \mathbf{x} are defined as

$$\mathbf{x} = (\mathbf{y}_i(i = 0, \dots, n), \mathbf{u}^i(i = 0, \dots, n - 1), T)^T, \quad (74)$$

i.e. they include the state values at the grid vertices, the control values on each grid element and, possibly, the final time. The cost function and all problem constraints and bounds, including equations (73), are expressed in terms of the NLP variables \mathbf{x} to yield the finite dimensional optimization problem (72).

3.5 Methods Employed to Improve Convergence

The convergence to a feasible solution is typically found to exhibit a dependence on the initial guess supplied to the optimization subroutine. In order to supply a good initial guess to the optimization subroutine or to make the procedure more robust in general, the techniques described below were employed.

3.5.1 Bootstrap technique

For greater robustness of the optimization procedures, it is usually convenient to start from rather crude temporal discretizations. In fact, on a coarse grid certain details of the solution will not be captured, and this will usually imply a faster convergence of the NLP problem, especially if the initial guess is poor, i.e. the tentative solution is far from the converged one. If a fine grid is used starting from a poor initial guess, the fine details captured by the grid will tend to slow down or even prevent convergence. An effective way of addressing this issue is the use of a refinement procedure. At first, an initial guess is computed on a crude grid, and the corresponding NLP problem is solved. The computed solution is then projected onto a finer grid and used as an initial guess for the subsequent NLP problem. The procedure is continued until sufficient grid refinement has been achieved to yield converged

results. Local grid refinement based on a-posteriori error estimates rather than uniform grid refinement can be used to optimize the use of computational resources. This feature however, has not been implemented in the present work. Instead we use a simple hierarchy of nested uniform grids. We start on a mesh \mathcal{T}_h of constant uniform element size h , and we project onto a finer grid of $\mathcal{T}_{h/2}$ of uniform size $h/2$; m projections yield a final grid $\mathcal{T}_{h/2^m}$ of uniform size $h/2^m$.

A schematic diagram describing the bootstrap methodology is shown in figure 19. The crude or starting grid is called the parent grid and the refined or finer grid is called the child grid. The following rules are applied to obtain data for points on the child grid:

(1) Data on the refined grid for the first node is an average of a certain reference data (in this case, the trim controls for the vehicle corresponding to the starting state) and data from the first time step from the parent grid ($\frac{\delta_T + \delta_1}{2}$).

(2) Data for even numbered nodes (δ_{2n}) is set to be equal to data from the corresponding parent node (δ_n).

(3) Data for odd numbered nodes (δ_{2n+1}) is an average of the data from the preceding and succeeding nodes ($\frac{\delta_{2n} + \delta_{2n+2}}{2}$).

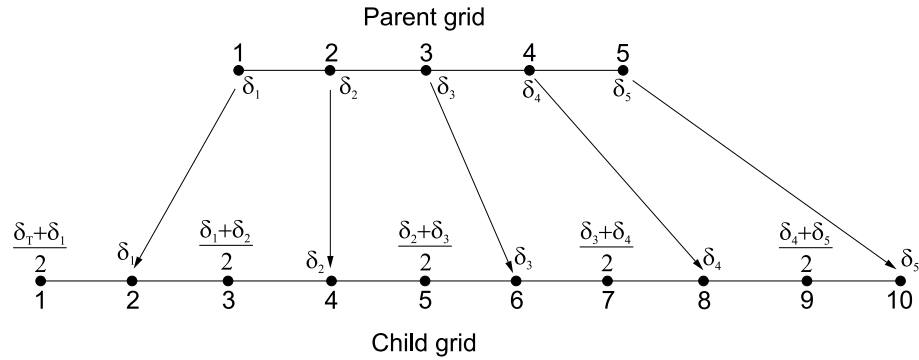


Figure 19: Schematic diagram explaining bootstrap procedure.

In essence, when we execute the bootstrap algorithm we are doubling the grid density by inserting interpolated points halfway between parent grid points. An example of bootstrap procedure is shown in figure 20 where the fin control deflections from a coarser grid are being projected onto a finer child grid. In figure 21 we see the improvement in accuracy of

the final solution for pitch angle as a result of using the bootstrap technique.

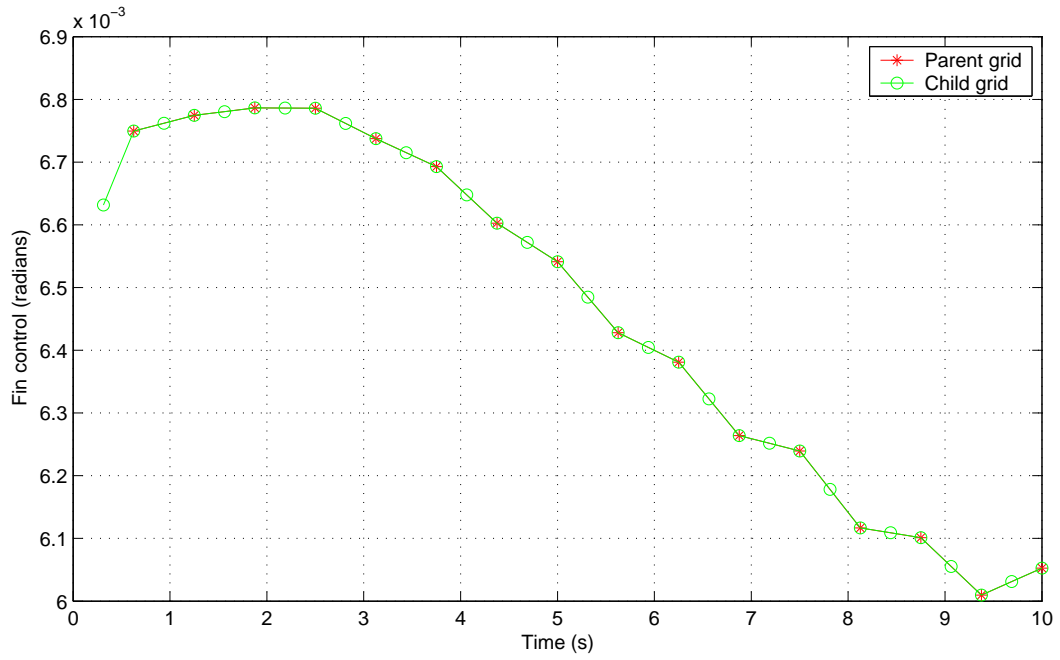


Figure 20: Bootstrap procedure projecting data onto finer grid.

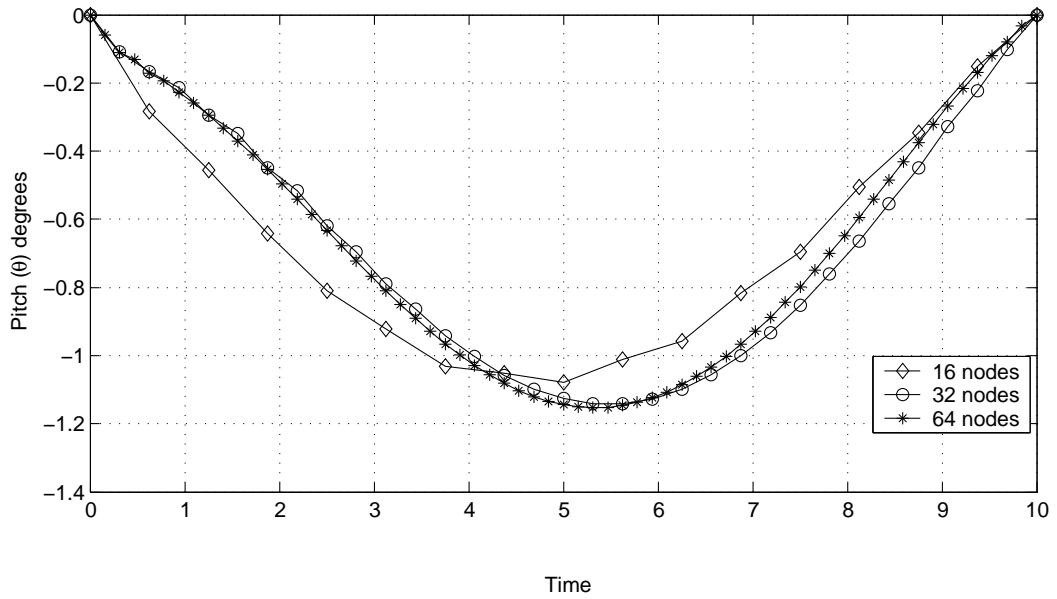


Figure 21: Convergence of solution as a result of bootstrap technique.

3.5.2 Scaling the variables

An additional robustness issue is related to the scaling of unknowns in the numerical optimization procedures. These are in fact notoriously sensitive to badly scaled problems. To address this issue, we first write the governing equations (63) here again:

$$\dot{\mathbf{y}} - \mathbf{z}(\mathbf{y}, \mathbf{u}) = 0,$$

We now introduce a scaling of the unknowns in the problem as follows:

$$\tilde{\mathbf{y}} = \mathbf{S}^y \mathbf{y}, \tag{75}$$

$$\tilde{\mathbf{u}} = \mathbf{S}^u \mathbf{u}, \tag{76}$$

$$\tilde{t} = S^t t, \tag{77}$$

Here, $\mathbf{S}^y = \text{diag}(S_i^y), i = 1, \dots, n_y$, is a diagonal matrix of weights that scales the state variables with respect to one another and similarly $\mathbf{S}^u = \text{diag}(S_i^u), i = 1, \dots, n_u$ is the analogous scaling matrix for the controls. Finally, S^t is the scaling factor for time. (The scaling is not currently implemented but we plan to scale time in our future efforts.) The scaling coefficients are chosen so as to obtain states and controls that are all approximately of order $\mathcal{O}(1)$.

We now rewrite equation (63) in terms of the scaled variables as:

$$\mathbf{S}^{y^{-1}} \dot{\tilde{\mathbf{y}}} - \mathbf{z}(\mathbf{S}^{y^{-1}} \tilde{\mathbf{y}}, \mathbf{S}^{u^{-1}} \tilde{\mathbf{u}}, S^{t^{-1}} \tilde{t}) = 0. \tag{78}$$

Now in order to non-dimensionalize this equation we need to pre-multiply it with the scaling factor:

$$\mathbf{S}^y (\mathbf{S}^{y^{-1}} \dot{\tilde{\mathbf{y}}} - \mathbf{z}(\mathbf{S}^{y^{-1}} \tilde{\mathbf{y}}, \mathbf{S}^{u^{-1}} \tilde{\mathbf{u}}, S^{t^{-1}} \tilde{t})) = 0. \tag{79}$$

That is,

$$\dot{\tilde{\mathbf{y}}} - \mathbf{S}^y \mathbf{z}(\mathbf{S}^{y^{-1}} \tilde{\mathbf{y}}, \mathbf{S}^{u^{-1}} \tilde{\mathbf{u}}, S^{t^{-1}} \tilde{t}) = 0. \tag{80}$$

Finally, we introduce the variable $\tilde{\mathbf{z}}(\tilde{\mathbf{y}}, \tilde{\mathbf{u}}, \tilde{t}) = \mathbf{S}^y \mathbf{z}(\mathbf{S}^{y^{-1}} \tilde{\mathbf{y}}, \mathbf{S}^{u^{-1}} \tilde{\mathbf{u}}, S^{t^{-1}} \tilde{t})$ to get:

$$\dot{\tilde{\mathbf{y}}} - \tilde{\mathbf{z}}(\tilde{\mathbf{y}}, \tilde{\mathbf{u}}, \tilde{t}) = 0. \quad (81)$$

Due to this re-scaling of variables we have a new cost function and new constraints, written in terms of the scaled variables:

$$\tilde{J} = \phi(\tilde{\mathbf{y}}, \tilde{\mathbf{u}}, \tilde{t})|_{\Gamma} + \int_{\tilde{\Omega}} L(\tilde{\mathbf{y}}, \tilde{\mathbf{u}}, \tilde{t}) dt. \quad (82)$$

$$\mathbf{g}(\tilde{\mathbf{y}}, \tilde{\mathbf{u}}, \tilde{t}) \in [\mathbf{g}_{\min}, \mathbf{g}_{\max}]; \quad (83)$$

and upper and lower bounds are written as:

$$\tilde{\mathbf{y}} \in [\tilde{\mathbf{y}}_{\min}, \tilde{\mathbf{y}}_{\max}], \quad (84)$$

$$\tilde{\mathbf{u}} \in [\tilde{\mathbf{u}}_{\min}, \tilde{\mathbf{u}}_{\max}]. \quad (85)$$

As an example, let us consider a typical badly scaled vector X as follows:

$$\begin{aligned} & [\mathbf{v}_P(1) \ \mathbf{v}_P(2) \ \mathbf{v}_P(3) \ \boldsymbol{\omega}(1) \ \boldsymbol{\omega}(2) \ \boldsymbol{\omega}(3) \ \mathbf{q}(1) \ \mathbf{q}(2) \ \mathbf{q}(3) \ \mathbf{q}(4) \ \mathbf{u}_P(1) \ \mathbf{u}_P(2) \ \mathbf{u}_P(3)]' \\ & = [85 \ 0 \ 0 \ 0.1 \ 0 \ 0 \ 1 \ 0 \ 0 \ 0 \ 850 \ 0 \ 100]' \end{aligned} \quad (86)$$

Here $\mathbf{v}_P, \boldsymbol{\omega}, \mathbf{q}$ and \mathbf{u}_P have the same definitions as given in chapter 2. Clearly there are differences of up to three orders of magnitude between the highest and lowest variables in this vector, which causes difficulties in the numerical optimization procedure. To remedy this problem a scaling matrix $\mathbf{S}^y = \text{diag}([0.01; 1; 1; 1; 1; 1; 1; 1; 1; 0.001; 1; 0.01])$ is chosen and this scaling of the variables makes them amenable to the optimization subroutine.

3.5.3 Method of “continuation”

The dependence on the starting guess of the convergence and the time taken to converge to a solution means that it is important to supply a good starting guess to the procedure to obtain satisfactory results. Typically for a simple maneuver that involves very little deviation from the initial straight line trim path (which the vehicle would have otherwise followed), a linear starting guess that connects initial and final positions will suffice. However, for a maneuver that involves significant effort and is far from the initial straight line trim path, a simple linear guess is often inappropriate and seldom leads to convergence.

In order to arrive at a converged solution for most extreme maneuvers we first develop of family of similar maneuvers starting with the trim path and ending in the maneuver of choice. For example if we want to find an optimal path that results in the vehicle diving by 60 m we start with a dive of 10 m and find solutions in increments of 10 m ending at 60 m. This ensures that the starting guess for the 60 m dive is the 50 m dive which is a much better guess than just a straight line joining the initial and final points of the trajectory.

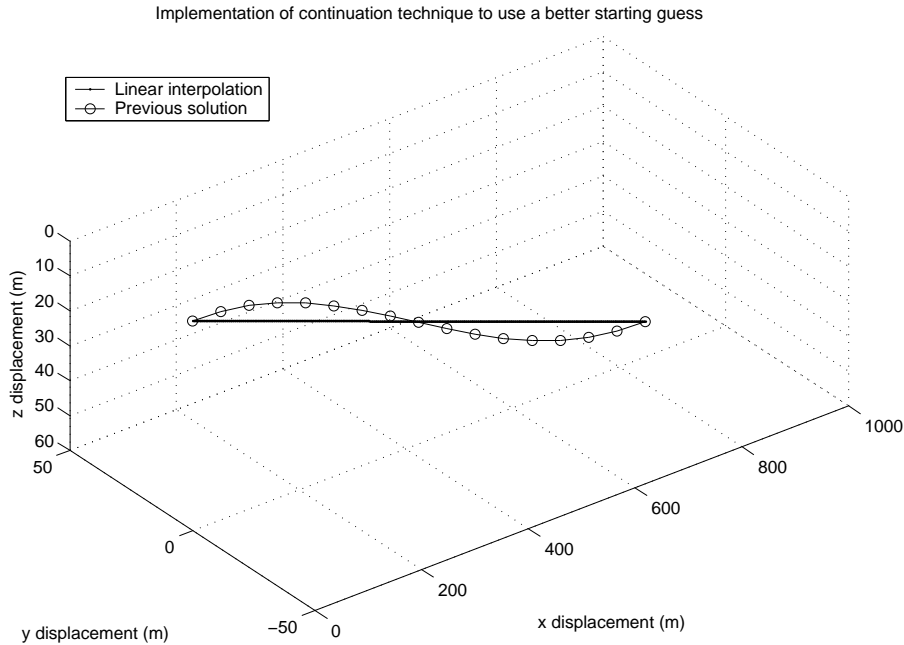


Figure 22: Application of continuation technique to arrive at dive of 60 m using a better starting guess (i.e. solution to 50 m dive problem).

3.6 TOMLAB and SNOPT

TOMLAB is a general purpose development environment for solving optimization problems. For any given optimization problem there are a number of solvers available that can be used to arrive at the desired solution, but TOMLAB provides a simplified interface that can call any available solver, hiding the details of the call from the user.

TOMLAB /SNOPT is the interface between The MathWorks' MATLAB and solvers developed by Stanford Systems Optimization Laboratory. In particular our optimization problem is a large-scale problem that contains many variables and constraints, many of

which are nonlinear. SNOPT requires relatively few evaluations of the problem functions as compared to other similar solvers and hence is more effective for our problem since the constraint functions in our case are expensive to compute.

Due to the nature of our problem, even though we have a large number of unknowns, each unknown appears in very few constraint equations. This means that our gradient matrices, the Jacobian and the Hessian, are quite sparse. In order to exploit the sparsity to speed up the optimization process, we specify the sparsity pattern of the Jacobian as a matrix of 1's and 0's, where 0 values indicate zeros in the constraint Jacobian and 1's indicate values that might be non-zero.

For example, consider the discretized system dynamics equations 73, rewritten here in functional form as follows:

$$\mathbf{f}(\mathbf{y}_{i+1}, \mathbf{y}_i, \mathbf{z}(\mathbf{y}_{i+1}, \mathbf{y}_i, \mathbf{u}^i)) = 0, \quad i = 1, \dots, n - 1.$$

Note that the only variables entering this equation are \mathbf{y}_{i+1} , \mathbf{y}_i and \mathbf{u}^i . Thus all other columns in the row of the Jacobian corresponding to this constraint will be zeros and only the columns corresponding to these 4 variables will be ones. See figure 23 for a representation of the sparsity pattern of the Jacobian for our problem. As a result of providing the sparsity pattern, the solver will not waste time trying to evaluate a constraint gradient by perturbing all of the unknowns. Instead only those unknowns that influence that particular constraint (as indicated by a non-zero value in the sparsity pattern) will be perturbed.

Further, for each iteration, the cost of evaluating the constraint gradients can be reduced by picking out only the particular constraints that are affected by the perturbed variable, instead of calculating all the constraints. For example, our constraint evaluation subroutine calculates the constraint for $N_{nonlconst} = n * n_{cont} + (n + 1) * n_{states}$ nonlinear constraints. Here n is the number of intervals, n_{cont} and n_{states} are the number of controls and states used (in our case $n_{cont} = 5, n_{states} = 13$). In the interest of efficiency, we want to avoid calculating all $N_{nonlconst}$ constraint violations when only a small number of the constraint violations need to be calculated in any given iteration. Hence we pass a flag which indicates that the i th variable is being perturbed and only the corresponding constraints that are

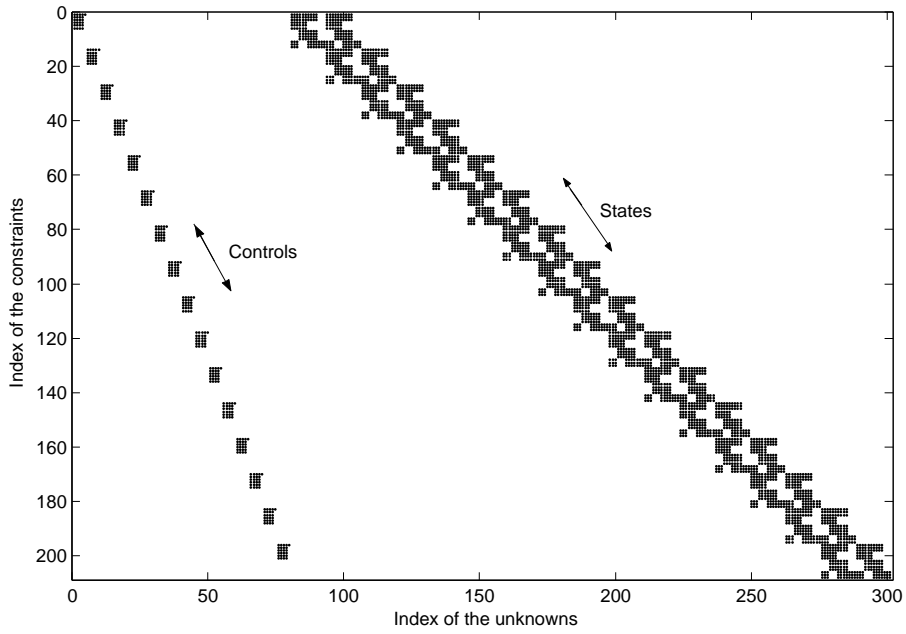


Figure 23: Sparsity pattern of the Jacobian matrix for our problem.

affected by this perturbation need to be computed.

Chapter IV

NUMERICAL SIMULATION AND RESULTS

4.1 Overview

The procedure outlined in the previous chapter is here tested on some representative maneuvers. The vehicle configuration used for these simulations reflects projected designs for a supercavitating torpedo. The vehicle is 4.0 m long and measures 0.2 m in diameter, and the cavitator is a circular disc of 0.07 m in diameter. The cruciform fin arrangement shown in figure 4 is considered. Fins 1 and 3 are oriented parallel to the axis of rotation of the cavitator and are used as elevators and ailerons, while fins 2 and 4 act as rudders and deflect by the same amount. The fins, located 3.5 m aft of the cavitator, feature a symmetric wedge shape which provides good strength characteristics as well as a transition between partial cavitation and supercavitation confined to a very limited range of deflection angles [13]. The total mass of the torpedo is 150 kg and is considered constant during flight. Future developments of this study will extend the current model to reflect mass reduction associated with fuel consumption and expulsion of ventilation gases. The configuration of the torpedo was summarized earlier in table 1. For practical applications it is important to ensure that the control time histories and the trajectories computed by the numerical optimization procedure are realizable and effectively flyable by a vehicle, at least within a reasonable engineering tolerance.

The vehicle flight envelope boundaries can be enforced through the use of appropriate constraints and bounds on the system state variables. Similarly, saturation of the controls can be imposed through constraints and bounds on the control variables themselves. However, in general this might not be sufficient for ensuring realistic solutions. In fact it should be realized that the flight mechanics models described in the previous sections lack critical components: the dynamics of the controls and control actuators are absent from the models.

This lack of modelling detail is typically acceptable in many flight mechanics applications

due to the fact that the characteristic time scales of the actuator dynamics are usually much smaller than the characteristic time scales of the vehicle dynamics. Thus a quasi-steady model can be used, where the controls \mathbf{u} become purely algebraic values that lack proper dynamics. As a result of adoption of this quasi-steady model the procedure is now blind to the intrinsic limitations of real actuators such as limited control velocities, limited actuation power etc. So without imposition of proper corrections the controls based on these incomplete flight mechanics models will typically show a characteristic bang-bang behavior, jumping from one saturation bound to the other. This implies very high or even infinite actuation speed and power which is unrealistic.

4.2 Control Effort

There are certain strategies that may be employed to ensure that realistic controls are obtained even with single-scale and incomplete flight mechanics models. One such simplistic strategy is to penalize an excessive “control effort.” This means that the difference between a reference trim control value and the controls required to perform the maneuver are penalized.

We attempt to find optimal trajectories with control effort as the cost function. Results are presented for dive and turn maneuvers. The cost function for the optimization is defined as

$$J = \int_{\Omega} (\mathbf{u} - \mathbf{u}_t) \cdot (\mathbf{u} - \mathbf{u}_t) dt, \quad (87)$$

where \mathbf{u}_t are the trimmed control values corresponding to the initial conditions.

4.2.1 Dive maneuvers

We consider a vehicle initially flying at trim conditions at a horizontal velocity of 85 m/s. We wish to find an optimal trajectory that involves diving to an assigned depth, with displacements constrained as follows: $\mathbf{u}_P(1) \in [0, 1000]$, $\mathbf{u}_P(2) \in [-100, 100]$, $\mathbf{u}_P(3) \in [0, z_T]$. Examples of the trajectories for final depth z_T varying between 10 m and 60 m are shown in figure 24 (note: positive $\mathbf{u}_P(3)$ points downward). The starting guess for the first dive maneuver is a straight line connecting initial and final positions. We then use a continuation technique whereby the trajectory for the previous optimization is used as a starting

guess for the next problem, thus generating a family of maneuvers. The total time for this maneuver is 10s. We choose a grid of 16 nodes on which our solutions are described.

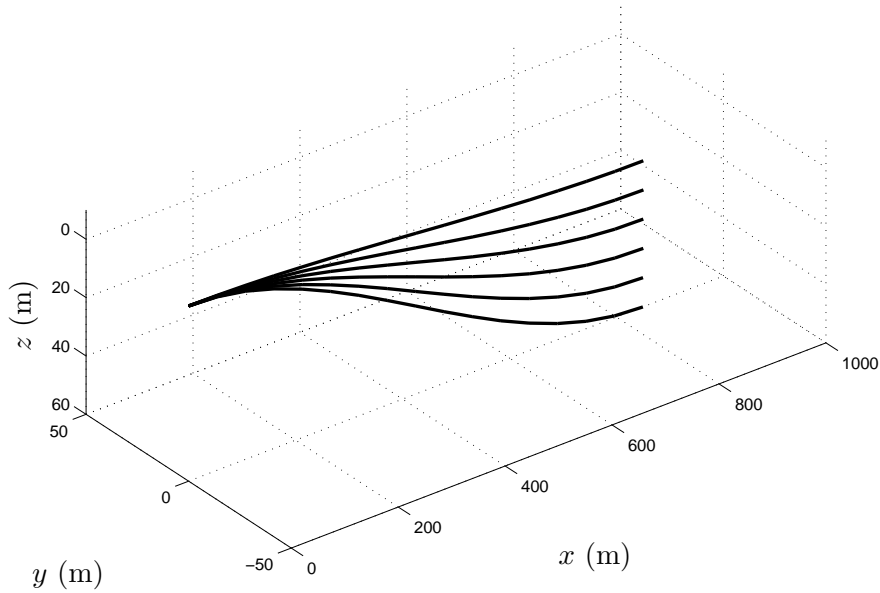


Figure 24: Family of dives with increasing final depth.

The time histories for the controls and the orientations are shown in figures 25 and 26. The controls remain steady throughout most of the simulation in order to keep the control effort at a minimum. However, they exhibit sharp jumps at the beginning and end of the maneuver in order to satisfy the initial and final conditions. The control deflections are marginally more pronounced in the case of the 60 m dive indicating that greater control forces are required to perform this maneuver. The rudder deflections are zero because the maneuver is in the \mathbf{b}_1 - \mathbf{b}_3 plane and no forces in the \mathbf{b}_2 direction are required. From figure 26 we see that the vehicle pitches down in order to perform the dive and then levels off to a horizontal orientation at the end to satisfy the condition that the vehicle finishes the maneuver flying horizontally.

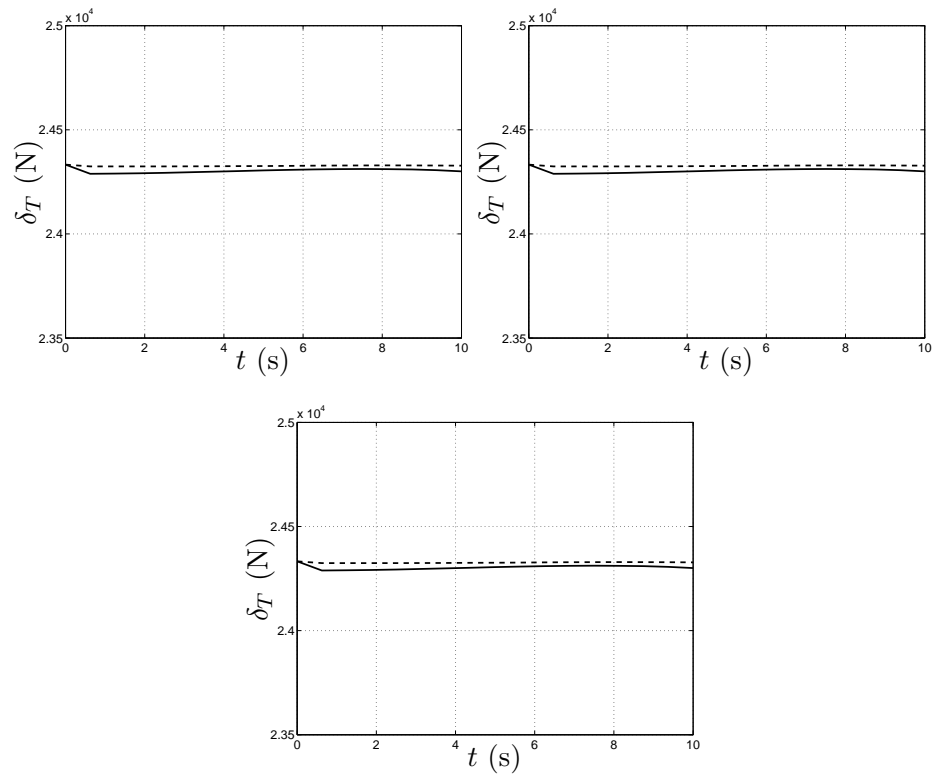


Figure 25: Control time history for 10 m (dashed line) and 60 m dives (solid line).

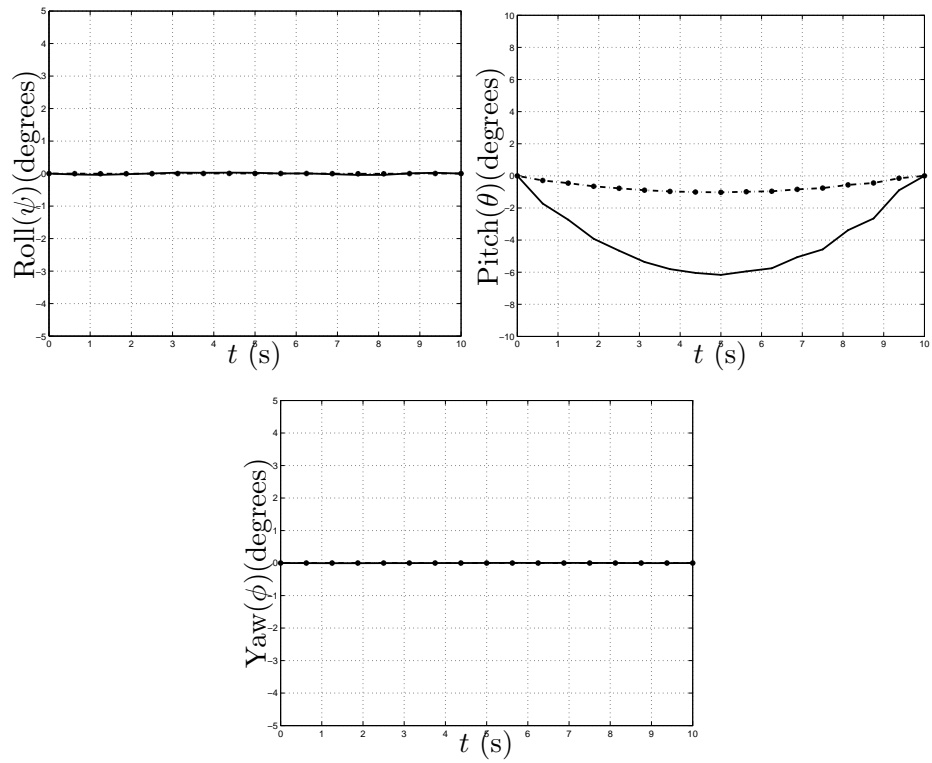


Figure 26: Inertial orientations for 10 m (dashed line) and 60 m dives (solid line).

4.2.2 Turn maneuvers

Shown in figure 27 is a family of turns for final inertial yaw orientations of 15, 30, 45, 60, 90, 120, 150 and 180 degrees with respect to the initial position. The final position along the \mathbf{b}_2 axis (the body-fixed axis that is initially parallel to the inertial \mathbf{i}_2 axis, see section 2.3) was left free but bounded, hence the turn simulation terminates at different \mathbf{b}_2 positions. The same bounds considered for diving are again imposed on the displacements, and the initial configuration of the vehicle again consists of trim conditions at 85 m/s horizontal velocity.

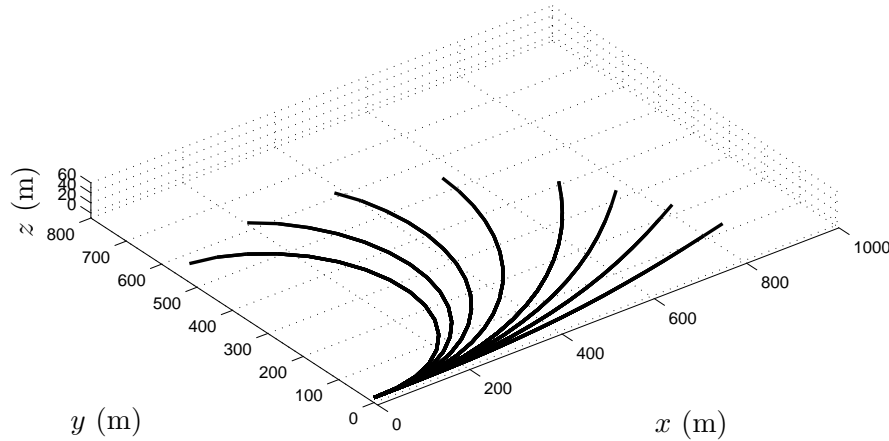


Figure 27: Vehicle trajectories for a family of turns

As a representative case as before, we present the time histories of the controls for the 15 degree and 180 degree turns in figure 28. We see significant rudder deflections in this case, which give rise to yawing moments required to execute the turn. The stabilizing fins also deflect considerably in order to provide a rolling moment so that a banked maneuver can be performed. The 180 degree turn requires much more control deflections than the 15 degree turn as expected.

The time history of the vehicle orientations, figure 29 shows how the vehicle banks to the right in order to execute a coordinated turn.

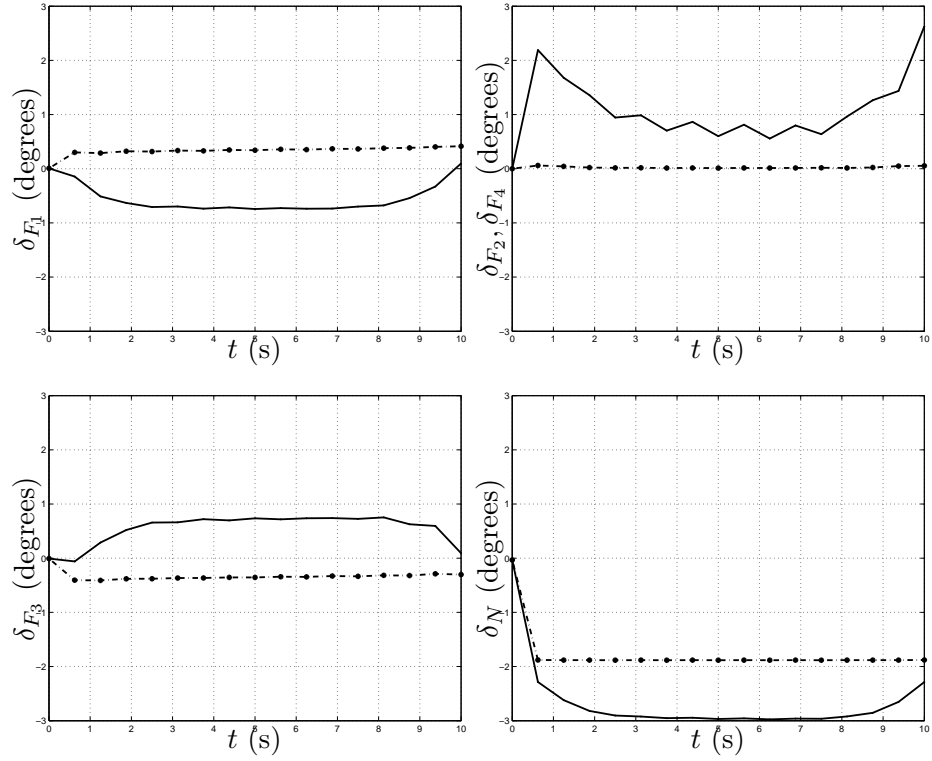


Figure 28: Control time history for 60° (dashed line) and 180° turns (solid line)

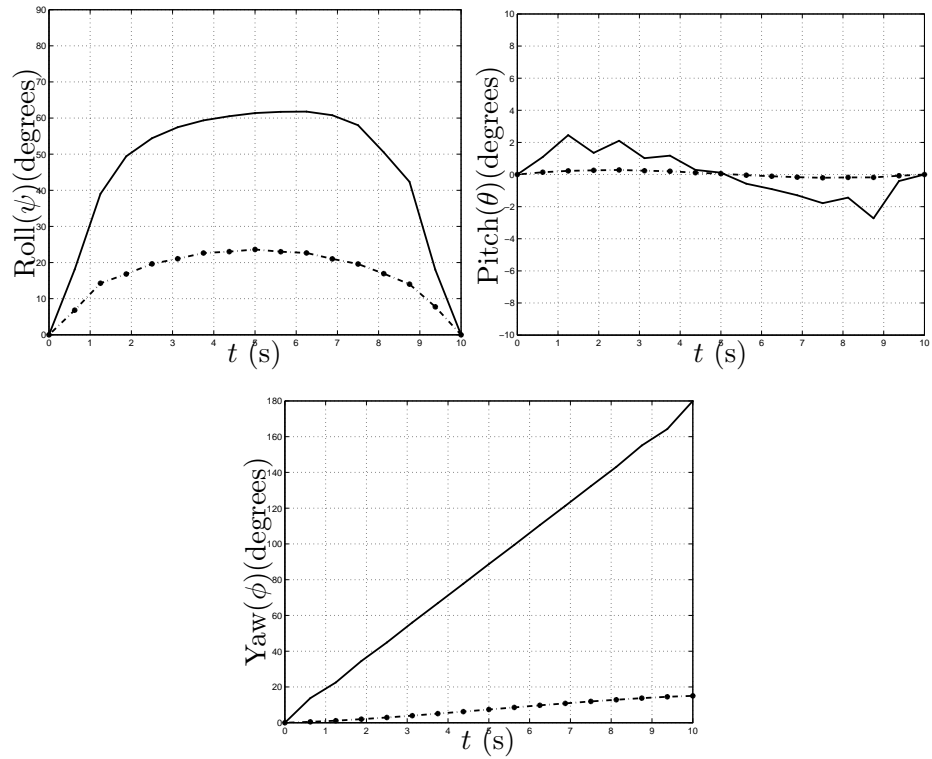


Figure 29: Inertial orientations for 60° (solid line) and 180° turns (dashed line)

4.3 Control Velocity

Another approach to ensuring that controls obtained as a result of the optimization are physically realistic is to use control velocities, $\dot{\mathbf{u}}$. These quantities are in reality subjected to physical limitations deriving from actuator dynamics as explained above. Introducing bounds on these quantities in the optimization problem, together with the saturation bounds, one can avoid the characteristic bang-bang type solutions in the computed controls. We would like to introduce this as an additional term in the cost function. Thus, the cost function for the optimization is defined as

$$J = w_1 \int_{\Omega} (\mathbf{u} - \mathbf{u}_t) \cdot (\mathbf{u} - \mathbf{u}_t) dt + w_2 \int_{\Omega} \dot{\mathbf{u}} \cdot \dot{\mathbf{u}} dt, \quad (88)$$

where w_1 and w_2 are weights assigned to control effort and control velocity respectively. For the numerical simulations the same torpedo configuration was used as given in table 1.

4.3.1 Dive maneuvers

We consider here the same family of maneuvers as calculated for the case of minimum control effort. The family of maneuvers is shown in figure 30 below. The continuation technique was used to find successive dives starting from the 10 m dive. The starting guess for the 10 m dive was the solution obtained for the 10 m dive with control effort as the objective function.

The time histories of the controls and orientations for 10 m and 60 m dives are shown in figures 45 and 44. In contrast to the control effort minimization case the controls here display less of a bang-bang behavior and are smoother except for the initial jump. This jump is only because the control velocity for the first jump involves difference between the first state to be optimized and the trim condition that the vehicle was flying at before the beginning of the maneuver, which has not been taken into account in the objective function.

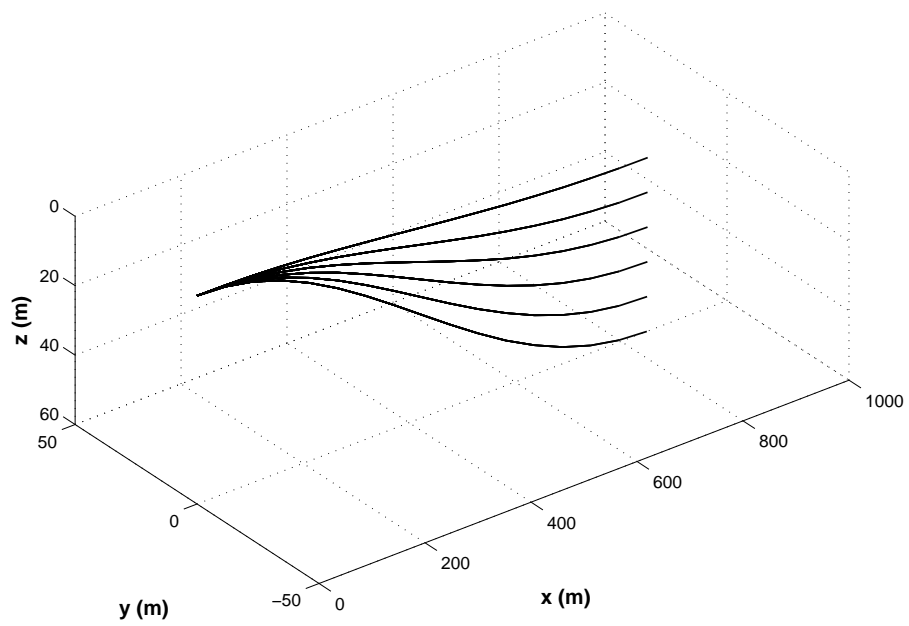


Figure 30: Vehicle trajectories for a family of dives with control velocity as the objective function

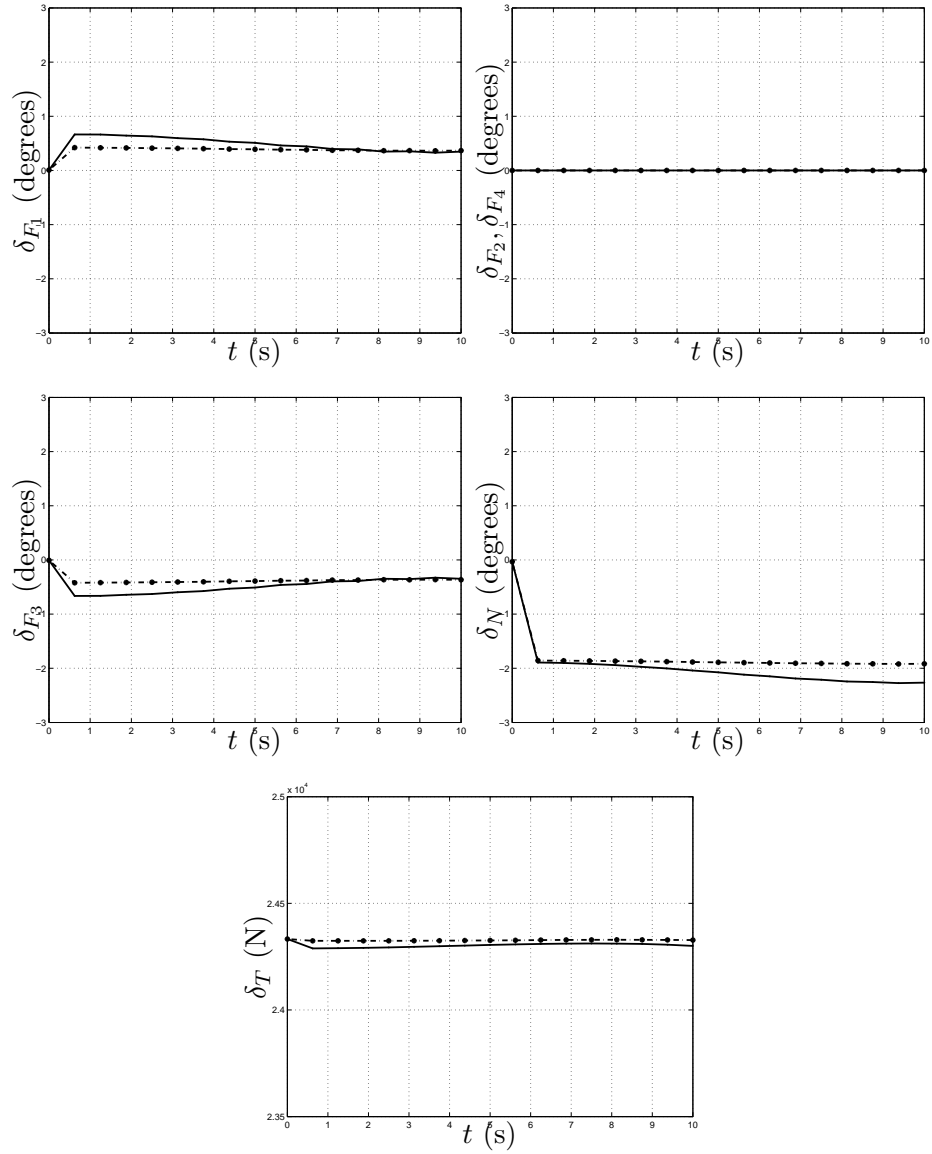


Figure 31: Control time history for 10 m (dashed line) and 60 m dives (solid line) for control velocity minimization case.

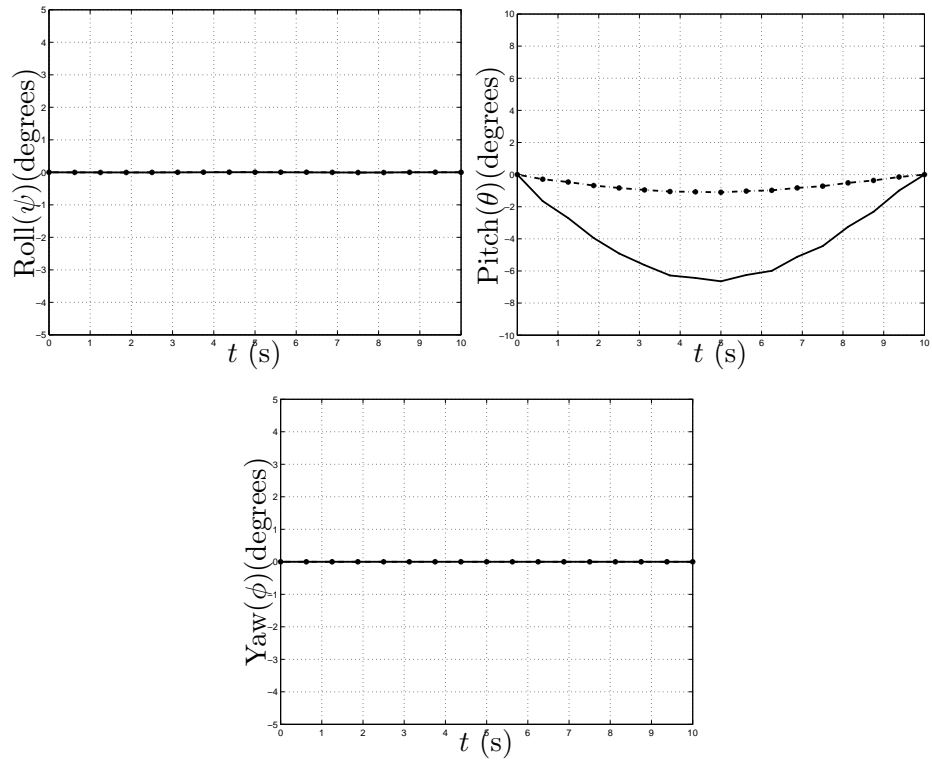


Figure 32: Inertial orientations for 10 m (dashed line) and 60 m dives (solid line) for control velocity minimization case

4.4 Comparison of Control Velocity and Control Effort Cases

It is of particular interest to compare the control time histories obtained from the control effort minimization case and the control velocity and effort minimization case to check if indeed the controls exhibit relatively lesser oscillations in the latter case. We compare the control time history of the 60 m dive for both cases to look for this behavior.

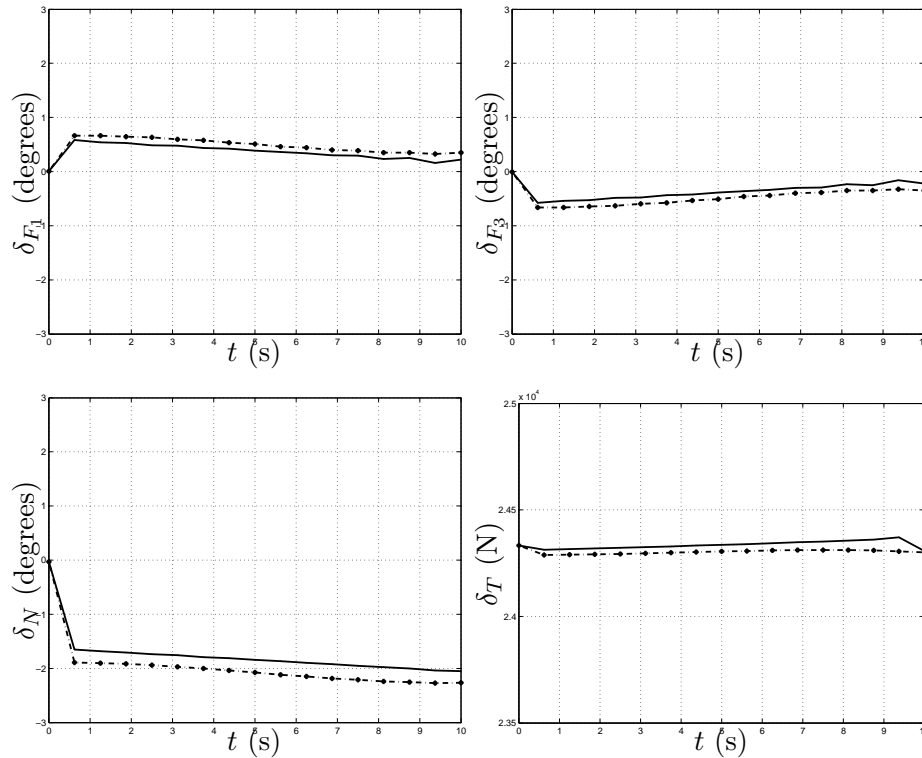


Figure 33: Control time history for 60 m dives with control velocity minimization (dashed line) and control effort minimization (solid line)

As expected, the control effort minimization problem yields a control time history which has lower control effort than the controls for the control velocity minimization problem, but is less smooth in comparison (consider the stabilizer deflections and thrust variations in figure 33).

4.5 Stationary Obstacle Circumvention

In practical situations the torpedo would have to navigate its way around obstacles, steering itself to clear the obstacle, and resume its initial heading. These obstacles could come in various shapes and forms, and the ability of the vehicle to avoid them provides a qualitative and realistic feel for the vehicle's maneuverability. In this study, we select stationary, infinitely long prismatic obstacles that may be of arbitrary (concave) cross-section.

4.5.1 Modelling the Obstacle

In order to account for any arbitrary cross-section of the obstacle, we develop a simple empirical method for modelling the obstacle. We enclose the arbitrary cross-section of the obstacle in an ellipse whose dimensions are calculated from the dimensions of the obstacle. The axes (a_x and a_y) of the ellipse are chosen to be 1.5 times the longest characteristic lengths, l_x and l_y (see figure 34) of the arbitrary cross-section along the \mathbf{i}_1 and \mathbf{i}_2 directions (recall from section 2.3 that the triad $\mathcal{I} = (\mathbf{i}_1, \mathbf{i}_2, \mathbf{i}_3)$ represents the inertial frame of reference). This ellipse fully envelops the obstacle and is a familiar surface that can be used to calculate constraint violations.

4.5.2 Formulation of Obstacle as a Constraint

In order to find a feasible trajectory that successfully avoids the obstacle, we need to mathematically model the obstacle as a constraint so that the optimization procedure can account for intersection of the trajectory with the obstacle. We introduce an additional constraint in the trajectory optimization problem formulation, which represents proximity to the obstacle.

One possible way to model the obstacle as a constraint would be to assign a single high penalty value (constraint violation) to any point on the trajectory that lies inside the obstacle. The resulting step function is shown in figure 35. However, note that this function is discontinuous at the boundary of the obstacle, and as a result, the gradients of the corresponding constraint at the boundary will be undefined. This makes it difficult for the optimization routine to find a feasible optimal solution to the obstacle avoidance

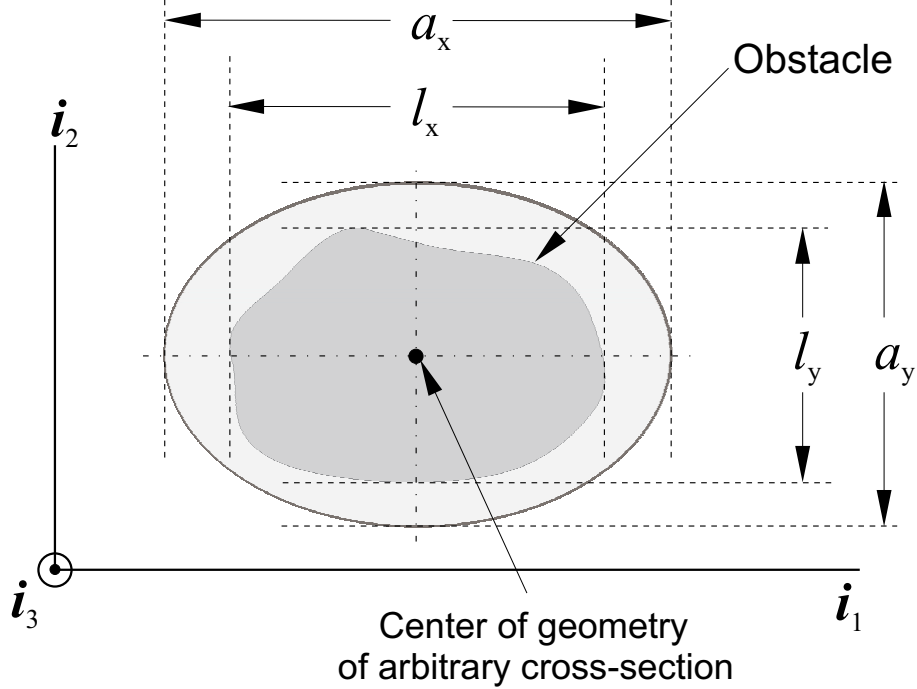


Figure 34: Enveloping the arbitrary cross-section in an ellipse

problem.

We see that the penalty value (constraint violation) assigned to any point on the trajectory needs to be a smooth and continuous function. There are a number of such functions available that satisfy this requirement, such as the sigmoid function and the Gaussian function. We choose the Gaussian function for its simplicity. The circular Gaussian function in two dimensions represents proximity to the obstacle. The function is written as follows [28]:

$$f(x, y) = \frac{1}{2\pi\sigma_x\sigma_y} e^{-[(x-\mu_x)^2/2\sigma_x^2 + (y-\mu_y)^2/2\sigma_y^2]}, \quad (89)$$

where μ_x and μ_y are the mean values in the i_1 and i_2 directions respectively about which the Gaussian function is symmetric, and σ_x^2 and σ_y^2 are the variances in those directions. To define the Gaussian function we need the point in space at which the function reaches its maximum (μ_x, μ_y) and the standard deviations (σ_x and σ_y), which define how quickly the function asymptotically approaches zero. Note that this approach can easily be extended to three dimensions by adding the appropriate terms in equation 89.

For our cylinder, the appropriate point would be where the cylinder's axis intersects the

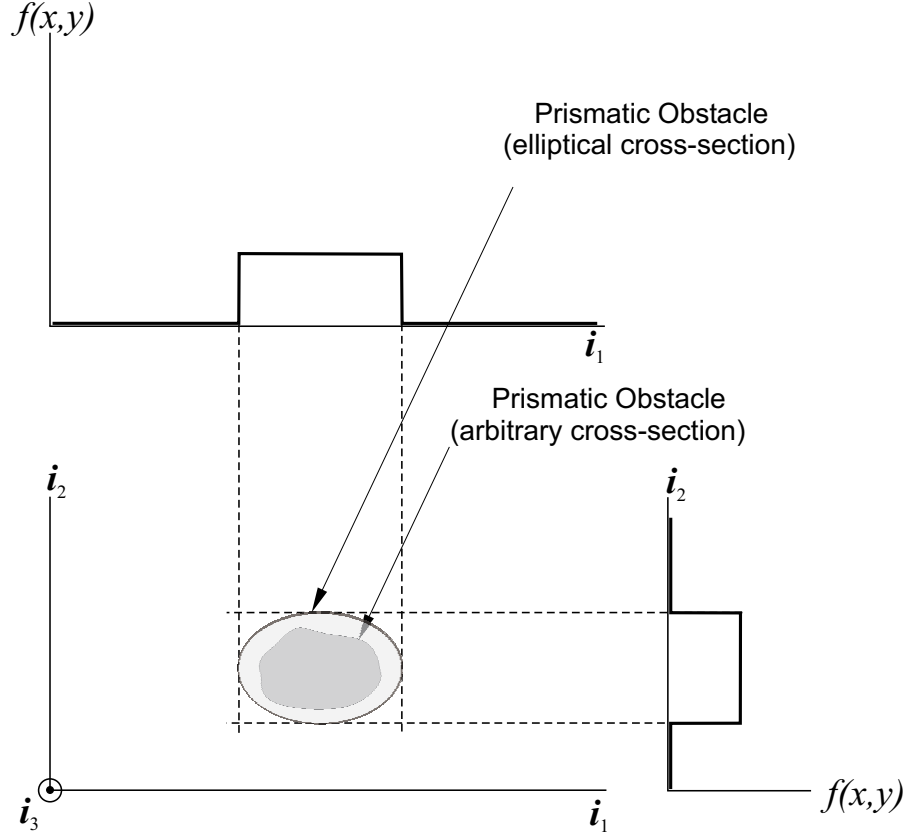


Figure 35: Using a step-function to assign trajectory constraint violation

i_1, i_2 plane. The full-width at half maxima ($W^{1/2}$) for the Gaussian function (the width of the bell-shaped curve between the two points where the function reaches half its maximum value) are set equal to the major and minor axes of the elliptical cross-section of the cylinder (see figure 36). Using the full-width at half maxima, the corresponding standard deviation can be easily derived as follows [28]:

$$\begin{aligned}\sigma_x &= \frac{W_x^{1/2}}{2\sqrt{2 \ln 2}}, \\ \sigma_y &= \frac{W_y^{1/2}}{2\sqrt{2 \ln 2}}\end{aligned}\tag{90}$$

where $W_x^{1/2}$ and $W_y^{1/2}$ are the full-width half maxima, or the dimensions of the axes of the ellipse in the i_1 and i_2 directions respectively.

Using these parameters the smooth continuous Gaussian function for the obstacle proximity constraint violation can be fully defined.

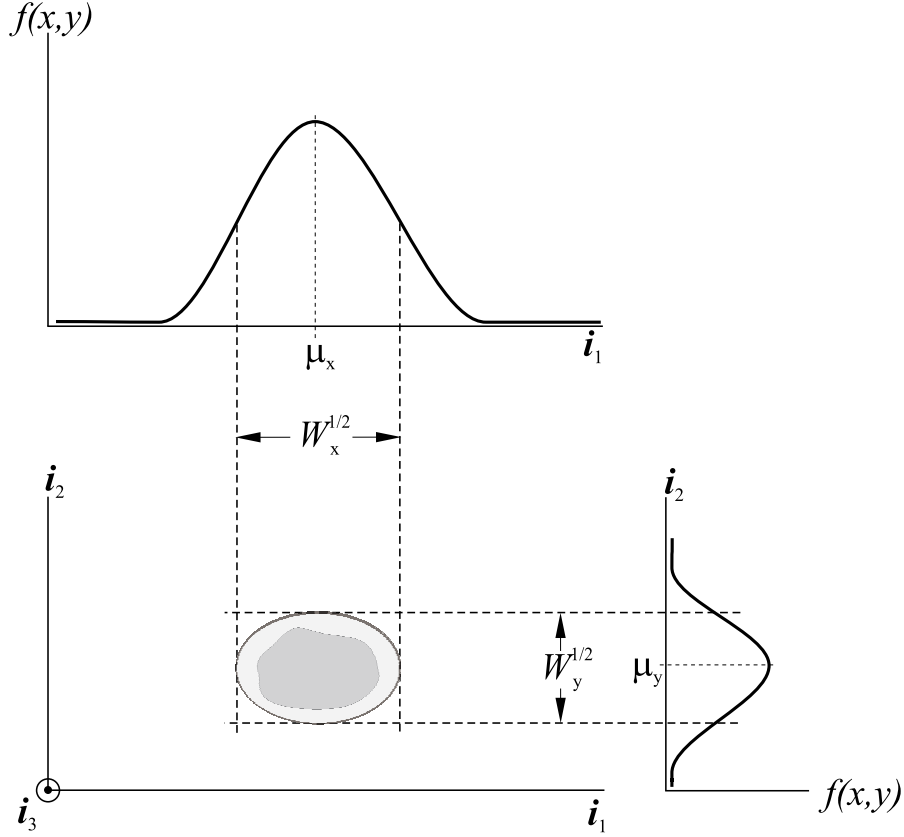


Figure 36: Using the Gaussian function to assign trajectory constraint violation

For each point on the trajectory we calculate value of the Gaussian function, $f_i(x, y)$. The Gaussian function value is the constraint that needs to be minimized (see figure 37):

$$\mathbf{g}_{obs}(\mathbf{y}, t) = f(x, y, t) \leq \Delta. \quad (91)$$

where $\mathbf{g}_{obs}(\mathbf{y}, t)$ is the constraint that needs to be satisfied, \mathbf{y} represents the states of the system, of which the constraint depends only on the inertial positions and t is the time at which the constraint is evaluated. Here $f(x, y, t)$ is the value of the Gaussian function at time t and x and y are the inertial positions on which the Gaussian function depends, which are a subset of the full state vector \mathbf{y} . Since the Gaussian function itself can never be exactly zero, writing this as an equality constraint could cause problems. Hence, we introduce a tolerance factor Δ which is a very small number (1e-6) so that the inequality constraint can be satisfied.

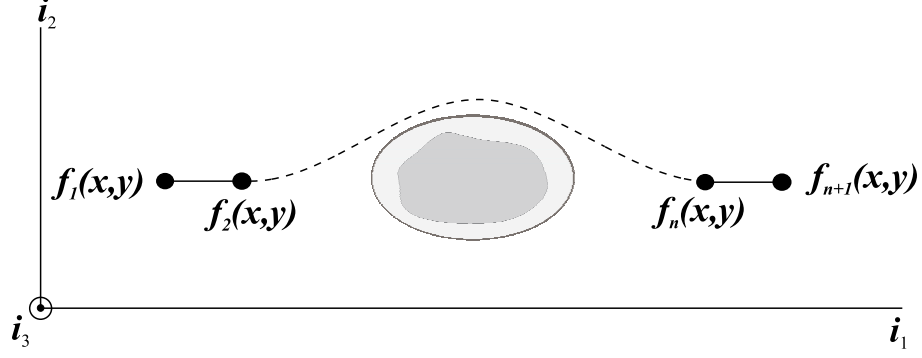


Figure 37: Gaussian function at each node of the grid

4.5.3 Vertical Infinite Elliptical Cylinder Obstacle Avoidance

Using the above formulation for an infinite elliptical cylinder obstacle we now solve a problem for a cylindrical obstacle whose axis is parallel to the inertial i_3 axis. The major and minor axes of the cylinder are chosen as 50 m and 30 m. The cylinder is placed at $(\mu_x = 500, \mu_y = 0)$. The Gaussian function for the $\mathbf{u}_P(3) = 0$ plane is shown in figure 38. We consider a vehicle initially flying at trim conditions at a horizontal velocity of 85 m/s. Displacements are constrained as follows: $\mathbf{u}_P(1) \in [0, 1000]$, $\mathbf{u}_P(2) \in [-100, 100]$, $\mathbf{u}_P(3) \in [-100, 100]$ (all measurements in meters). The objective function to be minimized is the control effort and the control velocity (equation 92):

$$J = w_1 \int_{\Omega} (\mathbf{u} - \mathbf{u}_t) \cdot (\mathbf{u} - \mathbf{u}_t) dt + w_2 \int_{\Omega} \dot{\mathbf{u}} \cdot \dot{\mathbf{u}} dt. \quad (92)$$

We set both weights w_1 and w_2 equal to 1. We also constrain the system to resume the initial trim condition and flight heading at the end of the maneuver. The initial guess is a simple straight-line path which the vehicle would follow if it were in trim flight. The resulting optimized solution is shown in figure 39.

The orientation of the vehicle as it performs this maneuver and the controls that yield this trajectory are shown below. We see that the vehicle performs a roll maneuver to avoid the obstacle, as indicated by the vehicle orientations and controls.

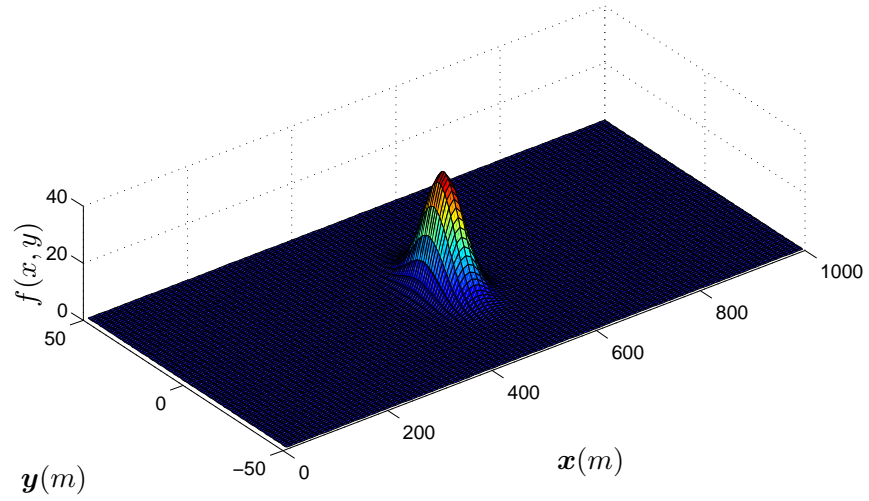


Figure 38: Gaussian function for an infinite elliptical cylinder obstacle in the $u_P(3) = 0$ plane

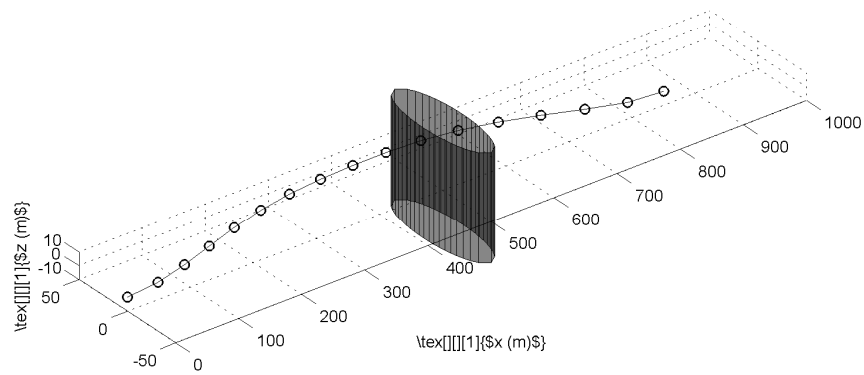


Figure 39: Feasible vehicle trajectory avoiding vertical cylindrical obstacle

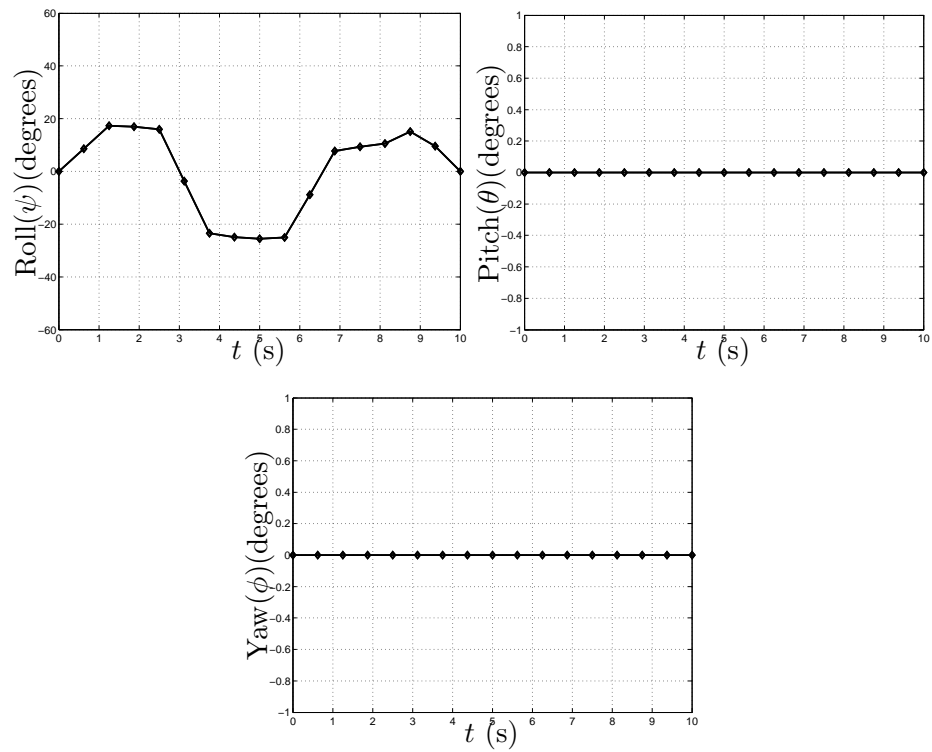


Figure 40: Inertial orientations for vertical cylinder avoidance case

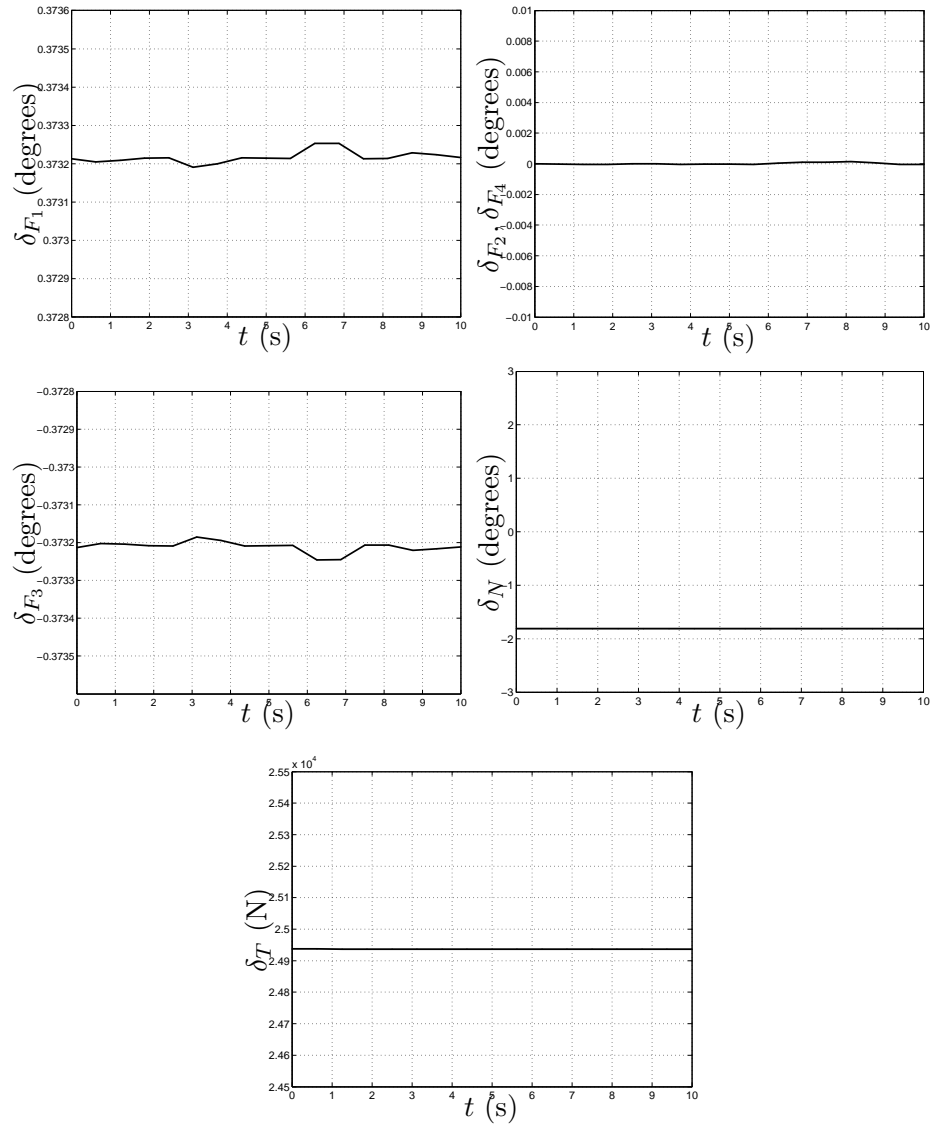


Figure 41: Control time history for vertical cylinder avoidance case.

4.5.4 Horizontal Infinite Elliptical Cylinder Obstacle Avoidance

Using the same formulation as before, for an infinite elliptical cylinder obstacle we now solve a problem for a cylindrical obstacle whose axis is parallel to the inertial \mathbf{i}_2 axis. The major and minor axes of the cylinder are chosen as 50 m and 30 m, as before. The cylinder is placed at $(\mu_x = 500, \mu_z = 0)$. The Gaussian function for the $\mathbf{u}_P(2) = 0$ plane is shown in figure 42. The optimized feasible path that minimizes the constraint violation corresponding to this Gaussian function is shown in figure 43.

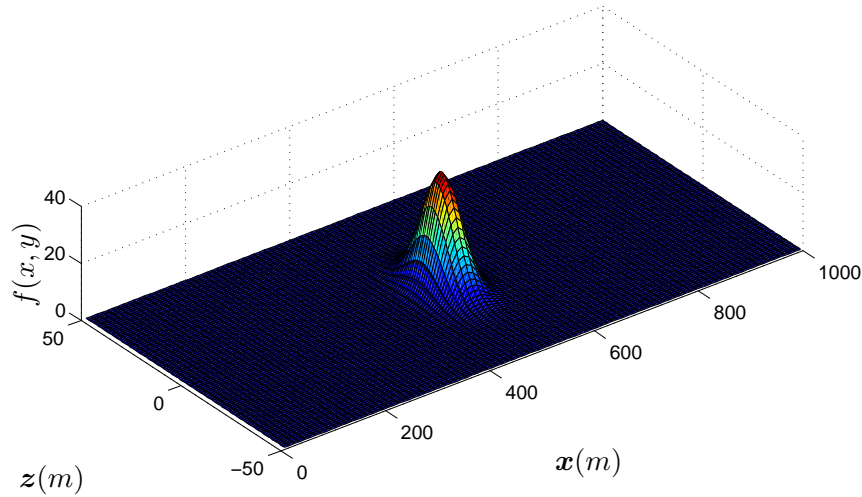


Figure 42: Gaussian function for an infinite elliptical cylinder obstacle in the $\mathbf{u}_P(2) = 0$ plane

The orientation of the vehicle as it performs this maneuver and the controls that yield this trajectory are shown below. The vehicle first pitches down and after clearing the maneuver pitches back up and finally ends at level horizontal flight. The vehicle performs a dive maneuver to avoid the obstacle, as indicated by the vehicle orientations and controls. Since control effort and control velocity both are being minimized, it appears that diving is a more efficient way to clear horizontal obstacles rather than climbing. This reinforces the concept that as the vehicle dives, shrinking of the cavity causes more fin immersion, which in turn increases fin effectiveness. The greater the fin effectiveness, the lesser the control effort required to perform the maneuver.

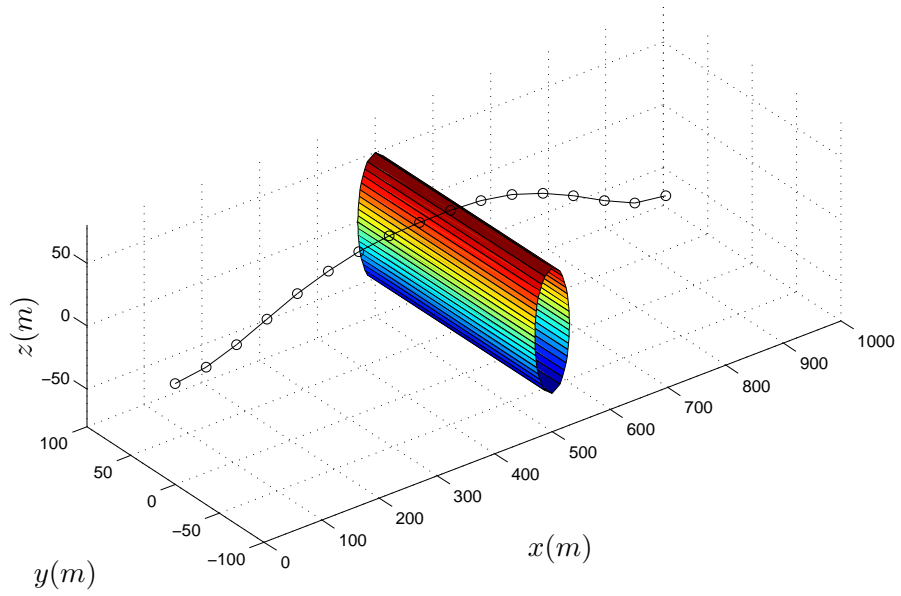


Figure 43: Feasible vehicle trajectory avoiding horizontal cylindrical obstacle

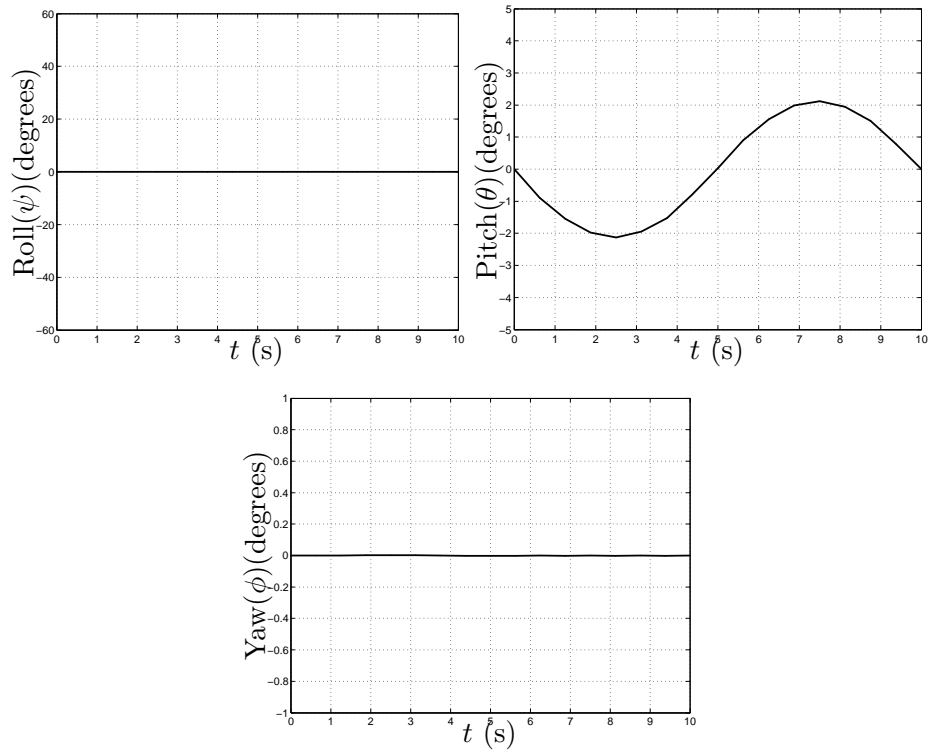


Figure 44: Inertial orientations for horizontal cylinder avoidance case

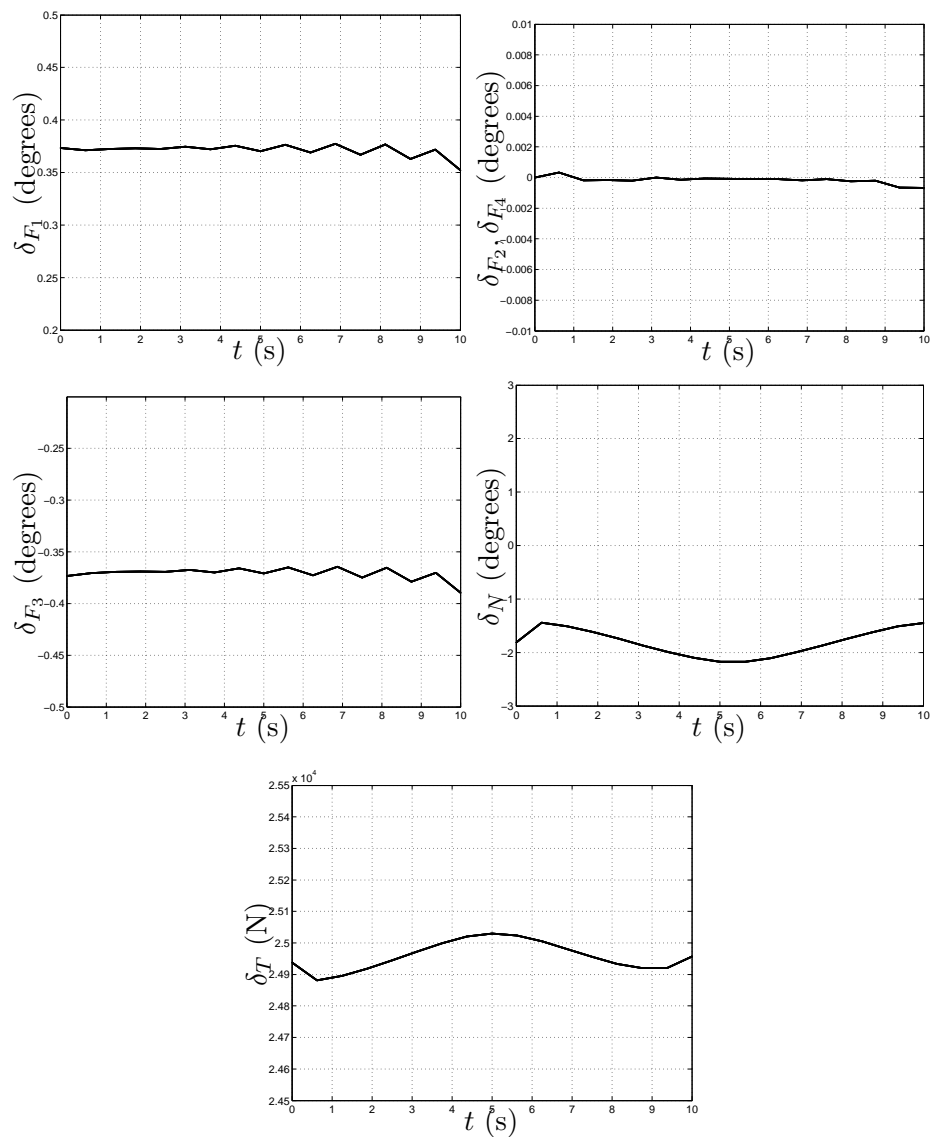


Figure 45: Control time history for horizontal cylinder avoidance case.

4.6 Effect of Cavitation Number on Maneuvers

As described earlier in chapter 2, the cavitation number σ is a measure of the tendency of cavitation to occur in a flow and as such, it is a principal quantity governing cavity dimensions. The definition, as given before and repeated here for convenience is:

$$\sigma = \frac{p_\infty - p_c}{1/2\rho v^2}$$

where p_∞, p_c are respectively the ambient and cavity pressures, v is the vehicles velocity and ρ is the fluid density.

The Reichardt equations for cavity dimensions are:

$$r_c(x) = \frac{d_{\max}}{2} \left[1 - \left(\frac{x/d_c - l_c/2d_c}{l_c/2d_c} \right)^2 \right]^{1/2.4} \quad (93)$$

where $r_c(x)$ is the cavity radius at location x , while d_{\max} and l_c denote maximum diameter and length of the cavity, respectively given by:

$$d_{\max} = d_c \sqrt{\frac{C_D(\sigma, 0)}{\sigma}} \quad (94)$$

$$l_c = d_c \sqrt{\frac{C_D(\sigma, 0)}{\sigma^2} \ln\left(\frac{1}{\sigma}\right)}, \quad (95)$$

where d_c is the cavitator diameter and $C_D(\sigma, 0)$ is the cavitator drag coefficient.

We see that both cavity length and radius depend on the cavitation number, which in turn depends on the ambient water pressure, p_∞ . This pressure varies with depth as $p_\infty = \rho hg$, where h is the depth below water surface and g is acceleration due to gravity.

From these relations it is obvious that as the depth increases, the ambient water pressure increases, causing an increase in σ . This in turn causes a reduction in the cavity dimensions d_{\max} and l_c . The variations of σ with depth and the variation of σ with velocity v are shown in figure 46. We also plot maximum cavity diameter versus σ and cavity length versus σ in figure 47. We note that as the cavity shrinks uniformly, the fin immersion depths consequently increase, resulting in greater effectiveness of the fins. It is interesting to study maneuvers at different depths underwater to see the effect of increased fin effectiveness on the control effort required to perform the maneuver.

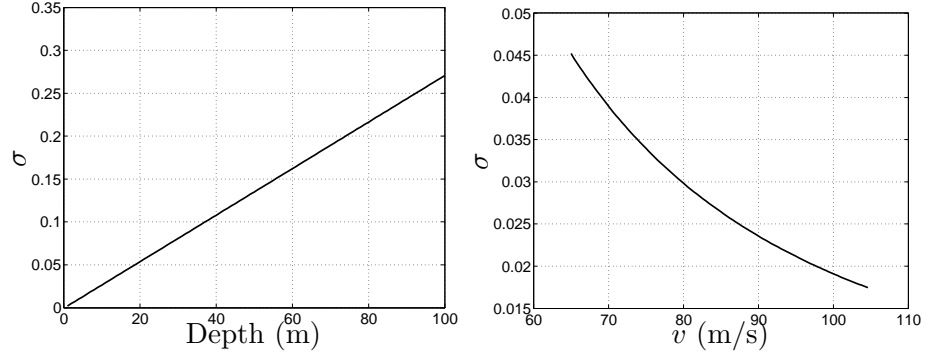


Figure 46: Variation of σ with increasing depth and increasing velocity

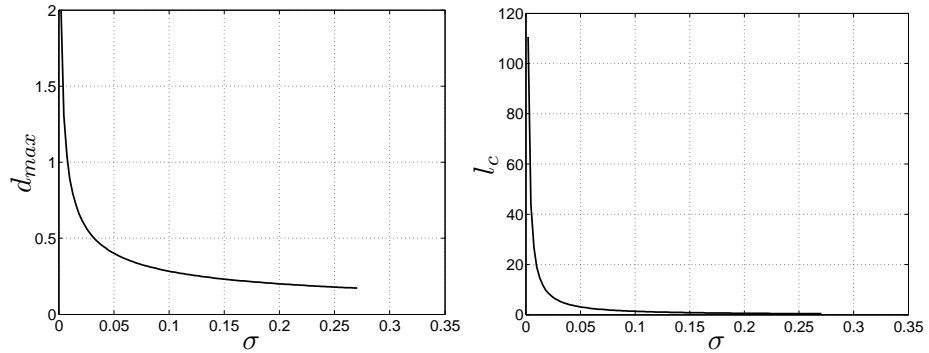


Figure 47: Variation of d_{max} and l_c with increasing σ

We now find optimal trajectories for a sample maneuver, in this case we choose a 15 degree turn, at different depths and we inspect the controls to see interesting trends. The trajectories obtained are shown in figure 49.

From the controls in figure 50 we see that maneuvers at greater depths require lesser control effort in general. This means that for more aggressive maneuvers it may be beneficial for the vehicle to dive to a certain depth to increase its maneuverability while maintaining forward velocity.

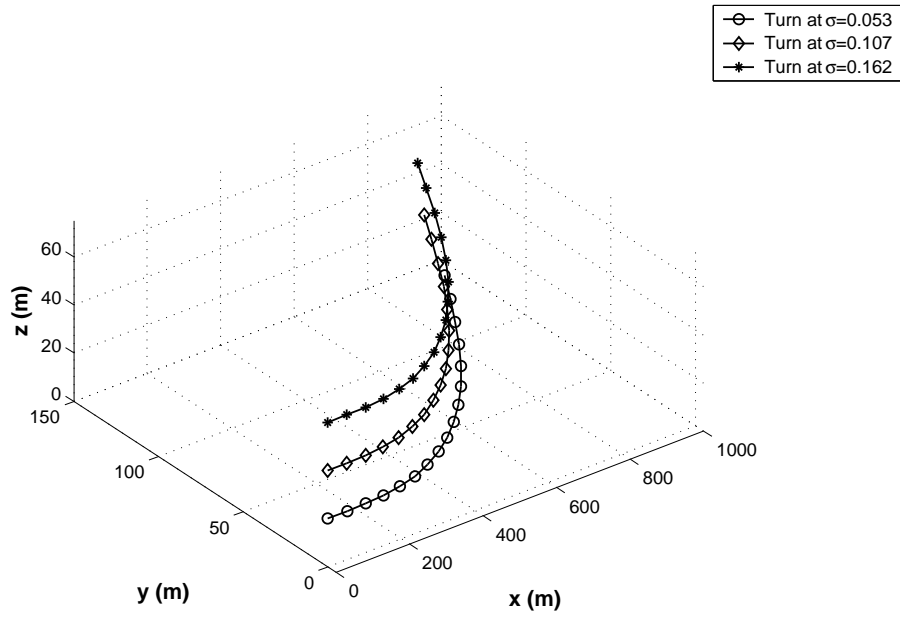


Figure 48: Variation of σ with increasing depth underwater (3-D plot)

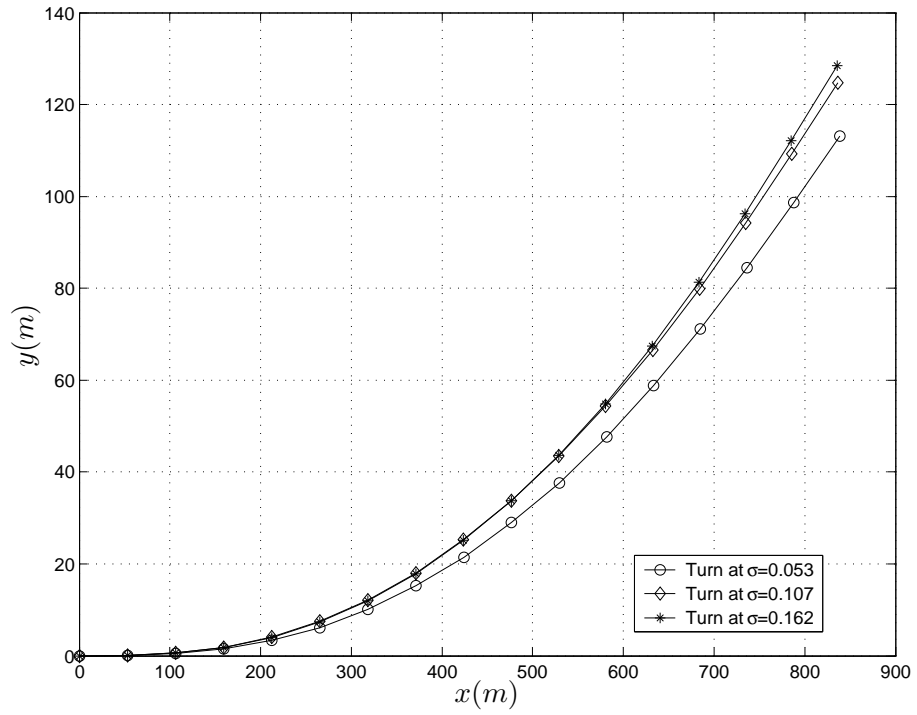


Figure 49: Variation of σ with increasing depth underwater (2-D plot)

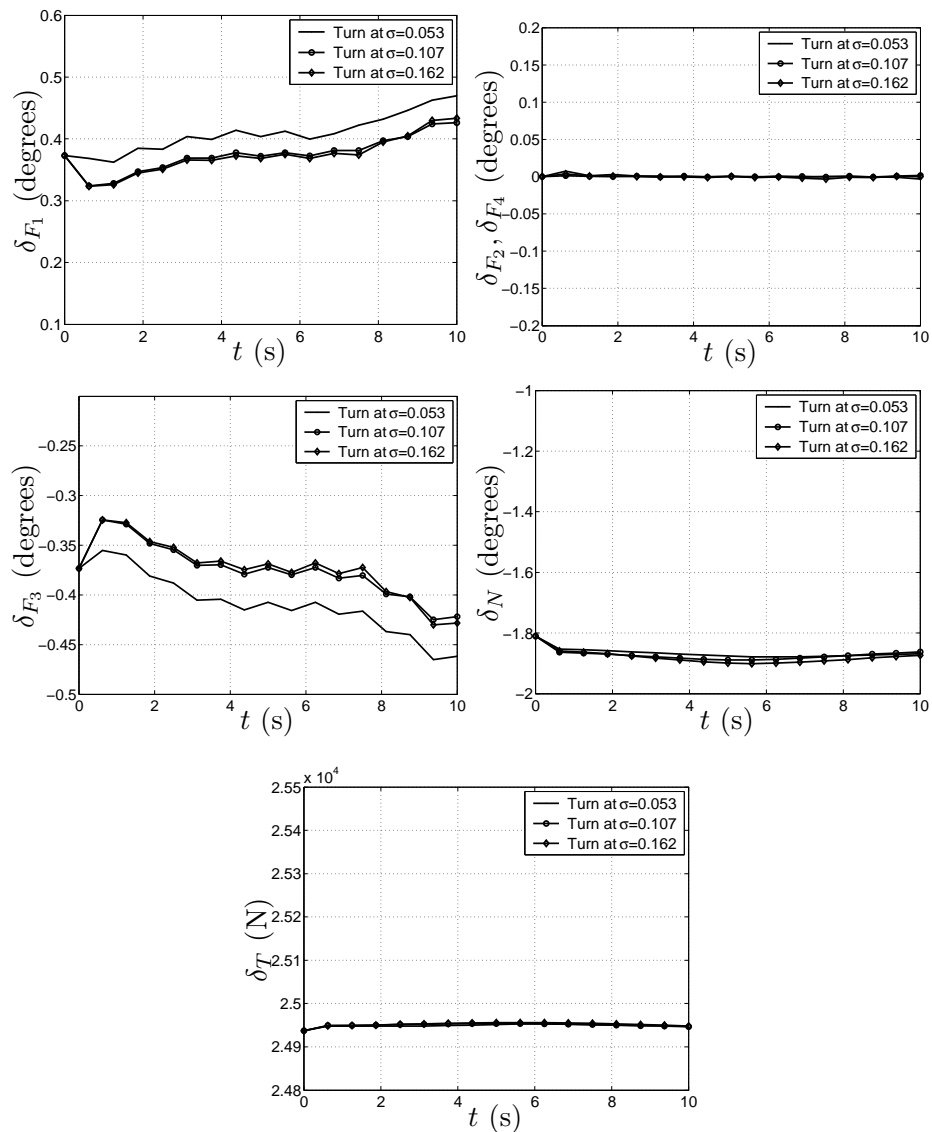


Figure 50: A 15 degree turn maneuver at varying depths.

Chapter V

CONCLUDING REMARKS

5.1 Conclusions

A framework has been developed for analyzing feasible trajectories for a supercavitating vehicle. We have defined the optimal control problem by assuming a certain vehicle configuration and specifying a cost function and constraints and bounds on the states and controls that translate the physical and operational requirements. The inherent sparsity of the system was exploited using a nonlinear large scale optimization software. We found the solution of this optimal control problem for two different classes of maneuvers and developed a family of feasible maneuvers for each class.

Further, we evaluated these two classes of maneuvers for two different types of objective functions, one involving minimization of control effort, the other involving minimization of control velocity. We observed that the control velocity optimization case gave more physical results that are compatible with the actuator dynamics and this compensates to some extent for the incompleteness of the mathematical model of the system.

Having developed the rigid-body flight mechanics simulator and the trajectory optimization framework, we then looked at utilizing these tools to study maneuverability of the vehicle by investigating its ability to avoid an infinitely long cylindrical obstacle. We cast the obstacle as a constraint violation and obtained feasible trajectories that avoid the obstacle and return to the initial heading and velocity.

We also studied the effects of varying the cavitation number σ on the maneuverability of the vehicle and observed that by increasing the depth of flight we can raise the value of σ and consequently cause the cavity to shrink, which increases the fin immersion depths. This makes the fins more effective, which means that more aggressive maneuvers can be performed without loss of forward velocity.

5.2 *Further Work*

Having developed the rigid-body flight dynamics simulator and the trajectory optimization framework, we can now look forward to using these tools to study vehicle performance, maneuverability and guidance and controls issues related to supercavitating vehicles. We outline below some of the proposed future work that could be conducted.

5.2.1 Complex maneuvers

The work done thus far can now be extended more complex maneuvers. An example of such a maneuver of interest is the startup maneuver where the vehicle begins from zero forward velocity and reaches steady trim velocity accompanied by the growth of the cavity. Other examples include 4-point hesitation roll, vertical loop and horizontal loop maneuvers. The latter group of maneuvers would have to be constructed by solving optimal control subproblems for simpler parts of the path separately and then joining these solutions together and using this as the starting guess for the full problem. Then, once a solution has been found it can be improved by increasing the grid density. The improved solutions can be run through the flight dynamics simulator to verify that the controls do indeed produce the desired trajectory.

5.2.2 Real-time controller

A real time controller is being developed, that tracks the trajectory and applies corrective control surface deflections to minimize the errors between the path followed and the path described. Further efforts would be aimed at comparing the effort with which this controller can track a feasible optimal path to the effort required to track an ad-hoc path selected between starting and final points. The effort required to track a feasible optimal path should ideally be much less, but this remains to be proven by the controller.

5.2.3 Investigating flight envelopes

We can now use this framework to investigate certain performance parameters of the vehicle, such as the maximum rate of climb that this vehicle can achieve. We can do this by successively decreasing the allowed horizontal displacement so that the vehicle has to execute

61 sharper climbs. A similar study can be performed to investigate the smallest turn radius achievable, given the vehicle configuration and operating conditions. Using a cost function such as minimization of control effort and control velocity will ensure that the controls obtained are realistic. Constraining the control surface deflections will ensure that the control time history obtained is attainable and can actually be implemented. Further, the constraints on the system states will ensure that the trajectories obtained are consistent with the vehicles equations of motion and with the model for forces and interactions for this complex system.

5.2.4 Flexible-body flight simulations

Once we have more feasible complex maneuvers calculated, we can run these results on the flexible-body forward flight simulator [10] and observe the differences in vehicle behavior and trajectory followed, if any. The flexibility of the vehicle introduces further non-linearities into the system such as vibrations due to after-body tail-slapping. It would be interesting to see the differences between the two models and the effect of introducing flexibility on the trajectory followed by the vehicle.

REFERENCES

- [1] Barclay, A., Gill, P.E. and Rosen, J.B., “SQP Methods and their Application to Numerical Optimal Control,” Report NA 97–3, Department of Mathematics, University of California, San Diego, CA, 1997.
- [2] Betts, J.T., “Survey of Numerical Methods for Trajectory Optimization,” *Journal of Guidance, Control and Dynamics*, Vol. 21, 1998, pp. 193–207.
- [3] Betts, J.T., *Practical Methods for Optimal Control Using Non-Linear Programming*, SIAM, Philadelphia, 2001.
- [4] Bottasso, C.L., Borri, M. and Trainelli, L., “Integration of Elastic Multibody Systems by Invariant Conserving/Dissipating Schemes. Part I Formulation,” *Computer Methods in Applied Mechanics and Engineering*, Vol. 190, 2001, pp. 3669–3699.
- [5] Bottasso, C.L. and Croce, A., “Optimal Control of Multibody Systems Using an Energy Preserving Direct Transcription Method,” *Multibody Systems Dynamics*, accepted, to appear.
- [6] Bottasso, C.L., Croce, A., Leonello, D. and Riviello, L., “Optimization of Critical Trajectories for Rotorcraft Vehicles,” *Journal of the American Helicopter Society*, under review.
- [7] Bottasso, C.L., Micheletti, S. and Sacco, R., “The Discontinuous Petrov-Galerkin Method for Elliptic Problems,” *Computer Methods in Applied Mechanics and Engineering*, Vol. 191, 2002, pp. 3391–3409.
- [8] Brodetsky, S., “Discontinuous fluid motion past circular and elliptic cylinders,” *Proceedings of the Royal Society*, A102 (as summarized in May, 1975).
- [9] Bryson, A.E. and Ho, Y.C., “Applied Optimal Control,” Wiley, New York, 1975.

- [10] Choi J.Y., Ruzzene M. and Bauchau O.A., “Dynamic Analysis of Flexible Supercavitating Vehicles Using Modal Based Elements,” *Proceedings of the International Mechanical Engineering Congress*, Washington DC, November 15–21, 2003.
- [11] Hassan, S., E., “Analysis of Hydrodynamic Planing Forces Associated With Cavity Riding Vehicles”, private communication, 2004.
- [12] Kirschner, I.N., Fine, N.E., Uhlman, U.S., Kring, D.C., Rosenthal, B.J., Gieseke, T.A., Kuklinski, R., Varghese, A.N., Stinebring, D.R., Dzielski, J.E., Lindau, J.W. and Kunz, R.F., “Supercavitation Research and Development,” *Undersea Defense Technologies*, Waikiki, HI, Oct. 2001.
- [13] Kirschner, I.N., Fine, N.E., Uhlman, J.S. and Kring, D.C., “Numerical Modeling of Supercavitating Flows,” *RTO AVT Lecture Series on Supercavitating Flows*, Von Karman Institute, Brussels, Belgium, Feb. 2001.
- [14] Kirschner, I.N., Kring, D.C., Stokes, A.W., Fine, N.E. and Uhlman, J.S., “Control Strategies for Supercavitating Vehicles,” *Journal of Vibration and Control*, Vol. 8, 2002, pp. 219–242.
- [15] Kulkarni, S., S., and Pratap, R., “Studies on the Dynamics of a Supercavitating Projectile,” *Applied Mathematical Modelling*, Vol. 24, No. 2, 2000, pp. 113–129.
- [16] Dzielski, J. and Kurdila, A., “A Benchmark Control Problem for Supercavitating Vehicles and an Initial Investigation of Solutions,” *Journal of Vibration and Control*, Vol. 9, Iss. 7, 2003, pp. 791–804.
- [17] Logvinovich, G. V., 1980, “Some problems in planing surfaces [sic],” translated from “Nekotoryyi voprosy glissirovaniya i kavitatsii [Some problems in planing and cavitation],” *Trudy TsAGI 2052*, Moscow, Russia.
- [18] Logvinovich, G. V., Buivol, V. N., Dudko, A. S., Putilin, S. I., and Shevchuk, Y. R., 1985, “Flows with free surfaces,” Naukova Dumka, Kiev, Ukraine (in Russian).

- [19] May, A., “Water Entry and the Cavity-Running Behavior of Missiles,” *Naval Sea Systems Command*, Arlington, VA, SEAHAC TR 75-2, 1974.
- [20] Miller, D., “Going to War in a Bubble,” *International Defense Review*, 1995, pp. 61-63.
- [21] Munzer, H. and Reichardt, H., “Rotational symmetric source-sink bodies with predominantly constant pressure distributions[sic],” *ARE Translation 1/50*, Aerospace Research Establishment, England (as summarized in May, 1975).
- [22] Rand, R., Pratap, R., Ramani, D., Cipolla, J. and Kirschner, I., “Impact Dynamics of a Supercavitating Underwater Projectile”, *Proceedings of DETC’97, 1997 ASME Design Engineering Technical Conferences*, Sept 14-17, 1997, Sacramento, California.
- [23] Reichardt, H., “The laws of cavitation bubbles at axially symmetrical bodies in a flow [sic]”, Ministry of Aircraft Production Volkenrode, MAP-VG, Reports and Translations 766, Office of Naval Research, Arlington, VA, 1946.
- [24] Renegar, J. “A Mathematical View of Interior Point Methods in Convex Optimization,” SIAM, Philadelphia, 2001.
- [25] Stinebring, D.R., Billet, M.L., Lindau, J.W. and Kunz, R.F., “Developed Cavitation-Cavity Dynamics,” *RTO AVT Lecture Series on Supercavitating Flows*, Von Karman Institute, Brussels, Belgium, Feb. 2001.
- [26] Sturgeon, V., “Racing Through Water: Supercavitation,” *Caltech Undergraduate Research Journal*, Vol. 1, No. 2, 2001, pp. 16-21.
- [27] Tulin, M., P., “Supercavitating flow past slender delta wings,” *Journal of Ship Research*, 3(3), 1959.
- [28] Weisstein, W., E., “Gaussian Function,” From *MathWorld* –A Wolfram Web Resource, <http://mathworld.wolfram.com/GaussianFunction.html>